PARAMAGNETIC RESONANCE STUDIES ON Mn (II) AND Fe (II,III) COORDINATED COMPLEX FERRATES

by

Ebru SOYSAL

A thesis submitted to

the Graduate Institute of Sciences and Engineering

of

Fatih University

in partial fulfillment of the requirements for the degree of

Master of Science

in

Physcis

June 2007
Istanbul, Turkey

APPROVAL PAGE

I certify that this thesis satisfies all the requirements as a thesis for the degree of Master of Science.

Prof. Dr. Mustafa KUMRU
Head of Department

This is to certify that I have read this thesis and that in my opinion it is fully adequate, in scope and quality, as a thesis for the degree of Master of Science.

Assist. Prof. Dr. Sadık GÜNER
Supervisor

Examining Committee Members

Prof. Dr. Mustafa KUMRU ……..

Assoc. Prof. Dr. Yüksel KÖSEOĞLU ……..

Assist. Prof. Dr. Ergün GONCA ……..

It is approved that this thesis has been written in compliance with the formatting rules laid down by the Graduate Institute of Sciences and Engineering.

Asst. Prof. Dr. Nurullah ARSLAN
Director

June 2007

PARAMAGNETIC RESONANCE STUDIES ON Mn (II) AND Fe (II,III) COORDINATED COMPLEX FERRATES

Ebru SOYSAL

M. S. Thesis - Physics
June 2007

Supervisor: Assist. Prof. Dr. Sadık GÜNER

ABSTRACT

Low temperature magnetic characterization on heterovalent Mn (II, III, IV) atoms including solid solutions of $LiMnO_2$-$LiGaO_2$ (2 mol % of Mn), $La_{0.75}Sr_{1.25}MnO_4$-$LaSrAlO_4$ (2 and 4 mol % of Mn) and Fe atoms including $LiFeO_2$-$LiGaO_2$ (5 mol % of Fe), $LiFeO_2$-$LiScO_2$ (5 mol % of Fe), $LaFeO_3$-$LaGaO_3$ (3 mol % of Fe) have been studied by Electron Paramagnetic Resonance (EPR) technique. The X-band (9.6-9.8 GHz) measurements have been performed in the temperature range of 5-300 K. The three magnetic phase transitions around 26, 51, 80 K and spin glass behavior are observed in the temperature regime of long range antiferromagnetic ordering for solid solution of $LiMnO_2$-$LiGaO_2$. Dipolar and exchange interactions between same and different ions play important role on line-broadening and absorption intensity characteristics of these complex powders. Mainly distorted octahedral symmetry has been determined for Mn^{2+} ions in the solid solution of $La_{0.75}Sr_{1.25}MnO_4$-$LaSrAlO_4$. The zero field splitting (ZFS) parameters, D = 490 Gauss due axial and E = 145 Gauss due orthorhombic terms have been obtained from theoretical calculations for Mn^{2+} ions. The transitions between corresponding energy levels have been specified for Mn^{2+} ions. Two magnetic phase transitions around 67 K and 105 K for two different concentrations of Mn have been observed. In addition to allowed transitions, the forbidden ΔM_S=2

transition originates from the Mn^{4+} ion has been observed below 14 K. The absorption intensity exhibits mainly Curie-Weiss like behavior for both types of complex oxides with decreasing temperature. For the ferrate type solid solution of $LiFeO_2$-$LiGaO_2$ it can be observed that there is a deviation from paramagnetic behavior between 25 K and 80 K. The zero field splitting (ZFS) parameters of Fe^{3+} including $LiFeO_2$-$LiScO_2$, have been obtained from theoretical calculations as A = 40 Gauss, D = 650 Gauss and E = 80 Gauss. Fe^{3+} ions are the paramagnetic source in the orthorhombic symmetry. Curie-Weiss type behaviors can be observed above 230 K and below 100 K because of ferromagnetic interactions. The perovskite type solid solution of $LaFeO_3$-$LaGaO_3$ has the polycrystalline ordering more than clustering.

Keywords: EPR, complex oxides, perovskite, ferrate, manganite.

Mn (II) ve Fe (II,III) BAĞLANTILI KOMPLEKS FERRATLARDA PARAMANYETİK REZONANS İNCELEMELERİ

Ebru SOYSAL

Yüksek Lisans Tezi - Fizik
Haziran 2007

Tez Yöneticisi: Yrd.Doç. Dr. Sadık GÜNER

ÖZ

$LiMnO_2$-$LiGaO_2$ (% 2 mol Mn), $La_{0.75}Sr_{1.25}MnO_4$-$LaSrAlO_4$ (% 2 ve 4 mol Mn) katı çözeltileri içerisindeki değişken değerlikli Mn (II, III, IV) atomlarının ve $LiFeO_2$-$LiGaO_2$ (%5 mol Fe), $LiFeO_2$-$LiScO_2$ (%5 mol Fe), $LaFeO_3$-$LaGaO_3$ (%3 mol Fe) katı çözeltileri içerisindeki Fe atomlarının düşük sıcaklıkta manyetik karakterizasyonu, Elektron Paramanyetik Rezonans (EPR) tekniği ile çalışıldı. X-band (9.6-9.8 GHz) ölçümleri, 5-300 K sıcaklık aralığında gerçekleştirildi. $LiMnO_2$-$LiGaO_2$ katı çözeltisi için, antiferromanyetik düzen sıcaklık sisteminde, 26, 51 ve 80 K civarında üç manyetik faz geçişi ve spin camsı davranışı gözlemlendi. Aynı ve farklı iyonlar arasındaki dipolar ve değiş-tokuş etkileşmeleri, kompleks tozların çizgi genişlemesi ve absorbsiyon şiddet karakteristiği üzerinde önemli rol oynar. $La_{0.75}Sr_{1.25}MnO_4$-$LaSrAlO_4$ katı çözeltisindeki Mn^{2+} iyonları için bozulmuş oktahedral simetri belirlendi. Mn^{2+} iyonları için sıfır alan yarılma parametreleri, D = 490 Gauss (eksen simetrisi) ve E = 145 Gauss (ortorombik simetri), teorik heseplamalardan elde edildi. Mn^{2+} iyonlarının enerji seviyeleri arasındaki geçişler belirlendi. Farklı Mn konsantrasyonları için 67 K ve 105 K de manyetik faz geçişleri gözlendi. İzinli geçişlere ek olarak, 14 K in altında Mn^{4+} iyonundan gelen yasak geçiş, $\Delta M_S=2$, gözlendi. Her iki kompleks oksit için, absorbsiyon şiddeti, azalan sıcaktıkta Curie-Weiss davranışı gösterir. Ferrat yapıdaki

$LiFeO_2$-$LiGaO_2$ katı çözeltisi için, 25 K ve 80 K arasında, paramanyetik yapıdan sapma gözlendi. Fe^{3+} içeren $LiFeO_2$-$LiScO_2$ için sıfır alan yarılma parametreleri teorik olarak A = 40 Gauss, D = 650 Gauss ve E = 80 Gauss bulundu ve ortorombik simetride paramanyetik kaynağın Fe^{3+} iyonu olduğu tespit edildi. Curie-Weiss davranışı, ferromanyetik etkileşmelerden dolayı 230 K üzerinde ve 100 K altında gözlenebilir. Perovskite yapıdaki $LaFeO_3$-$LaGaO_3$ katı çözeltisi küme yapısından ziyade polikristal yapıya sahiptir.

Anahtar Kelimeler: EPR, kompleks oksitler, perovskite, ferrat, manganat.

ACKNOWLEDGEMENT

I express my gratitude to my supervisor, Assist. Prof. Dr. Sadık GÜNER, whose help, advice, support and patience during my study.

I would like to express my thanks to Prof. Dr. Mustafa KUMRU and Assoc. Prof. Dr. Yüksel KÖSEOĞLU for their stimulating suggestions, encouragement and supports.

I also want to express my thanks to M. Mikhailova and N. Bobrysheva from Saint-Petersburg State University in Russia for the synthesis of my compounds, Prof. Dr. Bekir AKTAŞ from Gebze Institute of Technology for EPR measurements.

I want to express my thanks and gratitude to my family especially to my mother, Saime SOYSAL, for their motivation, supports and patience.

TABLE OF CONTENTS

LIST OF FIGURES

FIGURE

LIST OF TABLES

TABLE

LIST OF SYMBOLS AND ABBREVIATIONS

SYMBOL / ABBREVIATION

ESR	:	Electron Spin Resonance
EPR	:	Electron Paramagnetic Resonance
NMR	:	Nuclear Magnetic Resonance
μ	:	The electronic or atomic moment
T	:	Period
L	:	Angular Momentum Vector
S	:	Spin Vector
J	:	Total Angular Momentum Vector (**J** = **L** + **S**)
γ	:	Gyromagnetic ratio constant
B	:	Total Magnetic Field
H	:	Effective Magnetic Field
$\vec{\tau}$	:	Torque
ω	:	Angular frequency
ω_L	:	Larmour frequency
β_e	:	Bohr Magneton
$\hbar$	:	Constant ($\hbar$ = h /2π)
e	:	Charge of electron
m_e	:	Mass of electron
$\vec{M}$	:	Magnetization vector
$\vec{H}$	:	Applied magnetic field
χ	:	Magnetic Susceptibility
$\vec{r}$	:	Position operator
$\vec{p}$	:	Momentum operator

δ_{ij}	:	Delta function
L_+	:	Raising operator
L_-	:	Lowering operator
s	:	Spin quantum number
l	:	Orbital quantum number
j	:	Total angular momentum quantum number
m_s	:	Spin quantum number
m_l	:	Magnetic quantum number
m_j	:	Angular momentum quantum number
$\bar{\mu}_{total}$	:	Magnetic moment operator
g	:	Lande Splitting factor
H_{ze}	:	Electronic Zeeman interaction
H_{cf}	:	Crystal field interaction
O_k^q	:	Steven operator
B_k^q	:	Steven operator constant
D	:	Axial Zero Field Splitting parameter
E	:	Rhombic Zero Field Splitting parameter
μ_{nuc}	:	Nuclear magnetic moment
H_{hf}	:	Hyperfine interaction
A	:	Hyperfine interaction parameter
I	:	Nuclear spin
h	:	Planck's constant
υ	:	Frequency of the radiation
μ_B	:	Bohr Magneton
$\mathbf{B}_0$	:	Applied (external) Field
k	:	Boltzmann constant
I_0	:	Intensity of radiation
c	:	Sample concentration
ε	:	Absorption coefficient
a.u.	:	Arbitrary Unit
ΔH_{pp}	:	Line Width

λ	:	Symmetry parameter
$g_{\perp}$	:	Perpendicular component of g
$g_{\parallel}$	:	Parallel component of g
T_1	:	Spin-Lattice Relaxation Time
T_2	:	Spin-Spin Relaxation Time
G	:	Magnetic Field Unit, Gauss
T	:	Magnetic Field Unit, Tesla

CHAPTER 1

INTRODUCTION

The rechargeable lithium ion batteries are the most promising candidates as safe power sources with high energy density and good cycle performance. Many research groups have done investigations on various cathode materials for the lithium secondary batteries such as layered oxides; Li*M*O_2 (*M*: Mn, Fe, Ni, Co, …). Layered lithium transition metal oxides have a rock salt structure where Li and metal cation occupy the alternate layers (also identified as corrugated or zig-zag layers) of octahedral sites in a distorted close-package oxygen ion lattice [1].

One member of this type of materials is the orthorhombic $LiMnO_2$ (space group *Pmnm*) [2]. The low cost and less toxicity make Li and Mn based batteries more attractive [3]. The physico-chemical properties strongly depend on the preparation conditions. Especially, the structural defects determine the electrochemical activity of MnO_2 including oxide cathode materials. Due to presence of high-spin Mn^{3+} on the octahedral sites, the local site symmetry around Mn^{3+} is distorted from a regular octahedron by a cooperative Jahn-Teller distortion. The Mn sublattice is viewed as a folded triangular lattice, the fold angle being 111^0. Each triangle is distorted to isosceles with one edge of 2.80 A^o and the other two of 3.09 A^o [4]. The ordered salt like structure irreversibly transforms to a spinel ($Li_xMn_2O_4$) like cation ordering during electrochemical cycling [5, 6] Greedan *et al*. have reported for high temperature synthesized samples that long-range antiferromagnetic ordering is established below 261 K. They proposed a collinear magnetic structure based on antiferromagnetic interchain coupling along *a*-axis and antiferromagnetic interchain coupling considering that the nearest neighbor of Mn is another Mn along *a*-axis. The main disadvantage for orthorhombic $LiMnO_2$ is the small discharge capacity in the 4 V region, which is a great problem as a commercial candidate [7].

The Li and Fe based, $LiFeO_2$ is the most popular cathode material from the view-point of cost and nontoxicity [8]. There are three different forms of $LiFeO_2$ due to synthetic conditions and method. The α- $LiFeO_2$ is a cubic unit cell of space group *Fm3m*. β- $LiFeO_2$ is monoclinic, *C2/2* and formed by an intermediate phase during the ordering process. γ- $LiFeO_2$ is tetragonal, I41/amd and obtained by reducing the symmetry from cubic to tetragonal by ordering the Li^+ and Fe^{3+} ions at octahedral sites [9]. Kanno and co workers [10] found that the corrugated(zig-zag layered) structure of $LiFeO_2$ compound was electrochemically active during the Li insertion/extraction reaction. They synthesized the $LiFeO_2$ from γ-FeOOH using the H^+/Li^+ ion exchange reaction. Although this $Li/LiFeO_2$ cell exhibited a high discharge capacity of about 100 mAh/g and Li reversibly insertion/extraction in the FeO_2 layers, it shows a large capacity decline due to cationic disorder in the voltage region of 4.2-1.5 V.

Another type of metal oxides with general formula of ABO_3 (where the 12-coordinated A sites are rare or alkaline earth and 6-coordinated B sites are usually 3d transition metal cations) are called as perovskites. The main interest to investigate these materials as catalysts that can potentially replace noble metals for complete oxidation of hydrocarbons [11].

Due to great stability of perovskite framework a large number of trivalent cations can occupy the A and B sites provided that the tolerance factor *t* is in the range of 0.8-1.0. Furthermore, the perovskite composition can be widely changed by substituting either or both A and B site cations with other metals, which can also have an oxidation state different from 3+. In this case, formation of structural defects such as anionic or cationic vacancies and/or change in the oxidation state of transition metal cation arise in order to maintain the electroneutrality of compound. Such as $LaMnO_3$ may contain Mn^{4+} in addition to Mn^{3+} [12] or partial oxidation of Fe^{3+} and Fe^{4+} with formation of oxygen vacancies in $LaFeO_3$ have been reported [13]. The substitution in B site has also been investigated for $LaFeO_3$ by partially replacing Fe by Mg that has very close ionic radius. In that case the amount of Fe^{4+} reaches to maximum of 0.2 [14]. The crystal structure of $LaFeO_3$ is known to be orthorhombic with *Pnma* space group symmetry [15-18]. In the peculiar, the lattice symmetry changes from orthorhombic to nearly cubic. A charge disproportionation of Fe^{4+} is assumed to take place at low

temperatures in such compound, according to 2 $Fe^{4+} \rightarrow Fe^{3+} + Fe^{5+}$ [19]. Due to its nearly cubic symmetry and possible induced charge disproportionation, substituted $LaFeO_3$ perovskites may be more suitable for study of the intimate electronic interactions responsible for catalytic activity [20].

As for the single layered perovskite structure with general formula of $La_{1-x}Sr_{1+x}MnO_4$, $LaSrMnO_4$ is the mother compound and crystallizes in the K_2NiF_4 structure [21]. The $LaSrMnO_4$ is nominally undoped material, having Mn^{3+} sites and ideally no holes. Owing to the layered structure, the average octahedra are elongated along the *c*-axis. The orbital momentum of the Mn ions is quenched by the anisotropic crystal field and ferro-orbital ordering of $3z^2$-r^2 orbitals are realized [22]. The magnetization measurement study performed by C. Bauman et al showed that the $LaSrMnO_4$ reveals a magnetically inhomogeneous state [21]. On the other hand, there is a C-type AF spin order in agreement to the ferro-orbital order of predominantly $d_{3z^2-r^2}$ orbital. The single layered perovskite structures exhibit a strong Jahn-Teller distortion in which the Mn-O bond length along the *z*-axis is significantly larger than that in the *ab* plane, i.e., the MnO_2 plane.

The giant magnetoresistance in manganites with perovskite structure is another great interest for scientists [23]. Nano-dimensional local effects, such as cluster formation, electronic phase separation and charge ordering play important roles for giant magnetoresisting [24, 25]. These local effects are associated with superexchange interaction between Mn (III) and Mn (IV) atoms in perovskite structure.

The electron paramagnetic resonance (EPR) spectroscopy is very useful technique to investigate the electronic and magnetic states in solid samples. Moreover, it enables us to have information about symmetry around paramagnetic ion, local distortions or type of the heterovalent paramagnetic ions. In this study, the low temperature EPR analyses will be presented to explain the magnetic properties of the solid solutions for manganite $LiMnO_2$-$LiGaO_2$ with 2 % of Mn, ferrate $LiFeO_2$-$LiScO_2$ with 5 % Fe, ferrate $LiFeO_2$-$LiGaO_2$ with 5 % Fe, corrugated layer perovskite $LaFeO_3$-$LaGaO_3$, with 3 % of Fe, single layer perovskites $La_{0.75}Sr_{1.25}MnO_4$-$LaSrAlO_4$ with 2 and 4 % Mn.

CHAPTER 2

QUANTUM THEORY OF EPR

2.1. Introduction

Both in classical mechanics and quantum mechanics the magnetic moment μ and the angular momentum are proportional to each other. The current *I* carrying loop with an area of $A = \pi r^2$ in xy plane has a magnetic moment $\mu = iA$ in z direction. This is equivalent to that a particle of mass *m* and charge *q*, rotating with velocity $v = 2\pi r / T$ in a circular orbit of radius *r* in a period of *T*. The electrical current (charge flow per unit time) becomes $qv / 2\pi r$. Then the magnetic moment in a perpendicular direction to the plane of circle is

$$\mu = iA = \frac{qv}{2\pi r}\pi r^2 = \frac{qvr}{2} = \frac{q}{2m}L \qquad (2.1)$$

where $\vec{L} = m\vec{r} \times \vec{v}$ is the angular momentum. The magnetic moment is proportional to the resultant angular momentum **J** which is the summation of orbital angular momentum **L** and the spin angular momentum **S**. Therefore the above relation can be generalized as

$$\vec{\mu} = \frac{q}{2m}\vec{J} = \gamma\vec{J} \qquad (2.2)$$

where the proportionality constant $\gamma = q / 2m$ is called as magnetogyric constant. When a magnetic moment $\vec{\mu}$ is in a magnetic field **B** then the energy of the magnetic moment is $E = -\vec{\mu} \cdot \vec{B}$, this energy of interaction of magnetic moment and the magnetic field is called as Zeeman energy which will be considered with its details. As can be seen from

the relation, the energy is minimized when the magnetic moment lies along the magnetic field. There will be a torque $\tau = \vec{\mu} \times \vec{B}$ on the magnetic moment. Since the magnetic moment is associated with angular momentum and the torque is equal to the rate of change of angular momentum $\tau = d\vec{J} / dt$, the torque equation can be rewritten as [26]

$$\frac{d\vec{\mu}}{dt} = \gamma \vec{\mu} \times \vec{B} \tag{2.3}$$

Figure 2.1 shows the precession of magnetic moment around B field and its alignment in this field. The magnetic moment spin around magnetic field with and angular frequency of $\omega = \omega_L = -\gamma B$, this frequency is known as Larmor frequency.

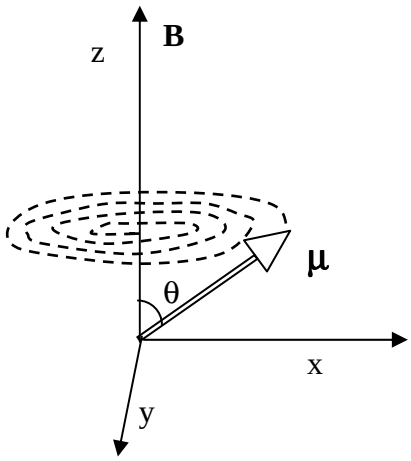

Figure 2.1 Precession of magnetic moment around magnetic field [26]

To calculate the size of magnetic moments, Bohr magneton β_e is defined. In Eq. 2.1 the angular momentum has the ground state value of $\hbar$. Then the magnetic moment for electron ($q = -e$, where e is elementary charge) is become

$$\beta_e = -\frac{e\hbar}{2m_e} = -0.927 \times 10^{-20} \, erg / gauss \tag{2.4}$$

and the magnetogyric constant for electron is $\gamma = -e / 2m_e$.

The magnetic solids consist of large magnetic moments. The magnetization $\vec{M}$ is defined as the magnetic moment per unit volume. Most solids are only weakly magnetic and develop a magnetization only when an external magnetic field is applied. In such cases, the amount of magnetization that is developed depends upon the magnitude of the magnetic susceptibility χ which is defined by

$$\vec{M} = \chi \cdot \vec{H} \tag{2.5}$$

where χ is susceptibility. Materials for which $\chi > 0$ are denoted as paramagnetic and $\chi < 0$ are diamagnetic. Materials with a spontaneous magnetization (i.e., which exhibit a magnetization $\vec{M}$ without application of a magnetic field) typically have much larger values for χ and can be either ferromagnetic, antiferromagnetic or ferrimagnetic. In the present chapter we focus on quantum theory of Paramagnetics and Electron Paramagnetic Resonance (EPR).

Magnetic moments in solids can be associated with both the conduction electrons and the ions (or closed shell valence electrons). In the case of electrons, magnetic moments are associated both with the orbital angular momentum and with the spin angular momentum of these electrons. To understand the intimate connection between magnetic moments and angular momenta, we review here a few basic definitions in quantum mechanics [27].

In classical mechanics and quantum mechanics, angular momentum is defined by

$$\vec{L} = \vec{r} \times \vec{p} = \begin{vmatrix} \hat{i} & \hat{j} & \hat{k} \\ x & y & z \\ p_x & p_y & p_z \end{vmatrix} \tag{2.6}$$

$$\begin{aligned} L_x &= yp_z - zp_y \\ L_y &= zp_x - xp_z \\ L_z &= xp_y - yp_x \end{aligned} \quad . \tag{2.7}$$

Since the position operator $\vec{r}$ and momentum operator $\vec{p}$ do not commute, the components of the angular momentum do not commute. We note first that the position and momentum operators do not commute:

$$(xp_x - p_x x) f(\vec{r}) = x\frac{\hbar}{i}\frac{\partial}{\partial x} f(\vec{r}) - \frac{\hbar}{i}\frac{\partial}{\partial x}[xf(\vec{r})] = -\frac{\hbar}{i} f(\vec{r}) = i\hbar f(\vec{r}) \tag{2.8}$$

This result is conveniently written in terms of the commutator defined by $[r_i, p_j] = r_i p_j - p_j r_i$ using the relation

$$[r_i, p_j] = i\hbar\delta_{ij} \tag{2.9}$$

where δ_{ij} is a delta function having the value unity if $i = j$, and zero otherwise. The Eq. 2.9 says that only the different components of $\vec{r}$ and $\vec{p}$ commute. If we now apply these commutation relations to the angular momentum we get:

$$[L_i, L_j] = i\hbar L_k \varepsilon_{ijk} \tag{2.10}$$

$$\vec{L} \times \vec{L} = i\hbar\vec{L} \tag{2.11}$$

$$[L_i, L^2] = 0 \tag{2.12}$$

It is convenient to introduce raising and lowering operators

$$L_{\pm} = L_x \pm iL_y \tag{2.13}$$

or

$$L_x = \frac{1}{2}(L_+ + L_-) \qquad \text{and} \qquad L_y = \frac{1}{2i}(L_+ - L_-) \tag{2.10}$$

The application of commutation relations to the raising and lowering operators gives:

$$[L^2, L_{\pm}] = 0$$

$$[L_z, L_{\pm}] = \pm\hbar L_{\pm} \tag{2.14}$$

$$[L_+, L_-] = 2\hbar L_z$$

Now by using the commutation relations above let's find the eigenvalues of the angular momentum matrices. One that diagonalizes both L_Z and L^2 and we will use quantum numbers m and ℓ to designate the representation as

$$\langle \ell m \mid L_z \mid \ell m' \rangle = m\hbar\delta_{m,m'} \tag{2.15}$$

$$\langle \ell m \mid L^2 \mid \ell m' \rangle = \ell(\ell+1)\hbar^2\delta_{m,m'} \tag{2.16}$$

$$\langle \ell m \mid L_+ \mid \ell m' \rangle = \frac{\hbar}{2}\sqrt{\ell(\ell+1) - m'(m'+1)}\,\delta_{m,m'+1} \tag{2.17}$$

$$\langle \ell m \mid L_- \mid \ell m' \rangle = \frac{\hbar}{2}\sqrt{\ell(\ell+1) - m'(m'-1)}\,\delta_{m,m'-1} \tag{2.18}$$

where ℓ orbital angular momentum quantum number and m can take $2\ell+1$ values ($m = -\ell, -\ell+1, \ldots\ldots, \ell$). All operators, the operator relations and the eigenvalues of these operators can be written for spin angular momentum and total angular momentum as orbital angular momentum:

Table 2.1 The operator relations and the eigenvalues of these operators for spin angular momentum and total angular momentum

$[S_i, S_j] = i\hbar S_k \varepsilon_{ijk}$	$[J_i, J_j] = i\hbar J_k \varepsilon_{ijk}$
$\vec{S} \times \vec{S} = i\hbar \vec{S}$	$\vec{J} \times \vec{J} = i\hbar \vec{J}$
$[S_i, S^2] = 0$	$[J_i, J^2] = 0$
$S_\pm = S_x \pm iS_y$	$J_\pm = J_x \pm iJ_y$
$S_x = \frac{1}{2}(S_+ + S_-)$	$J_x = \frac{1}{2}(J_+ + J_-)$
$S_y = \frac{1}{2i}(S_+ - S_-)$	$J_y = \frac{1}{2i}(J_+ - J_-)$
$[S^2, S_\pm] = 0$	$[J^2, J_\pm] = 0$
$[S_z, S_\pm] = \pm\hbar S_\pm$	$[J_z, J_\pm] = \pm\hbar J_\pm$
$[S_+, S_-] = 2\hbar S_z$	$[J_+, J_-] = 2\hbar J_z$
$\langle sm_s \mid S_z \mid sm_s' \rangle = m_s \hbar \delta_{m,m'}$	$\langle jm_j \mid J_z \mid jm_j' \rangle = m_J \hbar \delta_{m_j,m_j'}$
$\langle sm_s \mid S^2 \mid sm_s' \rangle = s(s+1)\hbar^2 \delta_{m,m'}$	$\langle jm_j \mid J^2 \mid jm_j' \rangle = j(j+1)\hbar^2 \delta_{m_j,m_j'}$
$\langle sm_s \mid S_+ \mid sm_s' \rangle = \frac{\hbar}{2}\sqrt{\ell(\ell+1) - m_s(m_s+1)}\,\delta_{m_s,m_s'+1}$	$\langle jm_j \mid J_+ \mid m_j' \rangle = \frac{\hbar}{2}\sqrt{j(j+1) - m_j(m_j+1)}\,\delta_{m_j,m_j'+1}$
$\langle sm_s \mid S_- \mid sm_s' \rangle = \frac{\hbar}{2}\sqrt{s(s+1) - m_s(m_s-1)}\,\delta_{m_s,m_s'-1}$	$\langle jm_j \mid J_- \mid jm_j' \rangle = \frac{\hbar}{2}\sqrt{j(j+1) - m_j(m_j-1)}\,\delta_{m_j,m_j'-1}$

An electron in an atomic state having orbital angular momentum $\vec{L}$ and spin angular momentum $\vec{S}$ can have its spin angular momentum coupled to the orbital angular momentum through the so-called spin-orbit interaction. Because of the orbital motion of the electrons, a magnetic field is created. Now this magnetic field acts on the magnetic moment associated with the electron spin and attempts to line up the moment along the magnetic field giving interaction energy and the hamiltonian

$$E_{SO} = \langle \psi \mid \xi \hat{L} \cdot \hat{S} \mid \psi \rangle \tag{2.19}$$

$$\hat{H}_{SO} = \frac{1}{2m_e c^2}\frac{1}{r}\left(\frac{\partial V}{\partial r}\right)\hat{L} \cdot \hat{S} = \xi \hat{L} \cdot \hat{S} \tag{2.20}$$

where V is the electrostatic potential on electron caused by atom. The total effects on an electron have to be defined so the effective potential on each electron in magnetic species or systems with many atoms [27].

$$\hat{H}_{SO} = \frac{1}{2m_e c^2}\sum_i \frac{1}{r_i}\left(\frac{\partial V_i}{\partial r_i}\right)\hat{L}_i \cdot \hat{S}_i = \sum_i \xi_i \hat{L}_i \cdot \hat{S}_i \tag{2.21}$$

To understand the splitting of energy levels due to spin-orbit coupling, eigen states and the eigenvalues of the system can be represented as

$$J^2 = (\vec{L}+\vec{S})\cdot(\vec{L}+\vec{S}) = L^2 + S^2 + 2\vec{L}\cdot\vec{S} \tag{2.22}$$

since $\vec{L}$ and $\vec{S}$ commute. The spin and orbital angular momenta commute because they operate in different vector spaces. Thus we obtain

$$\vec{L}\cdot\vec{S} = \frac{1}{2}\left(J^2 - L^2 - S^2\right) \tag{2.23}$$

and it can be written with its eigenvalue and state as

$$\vec{L}\cdot\vec{S}\left|\ell s\right\rangle = \frac{1}{2}\hbar^2\left\{j(j+1) - \ell(\ell+1) - s(s+1)\right\}\left|\ell s\right\rangle . \tag{2.24}$$

Because of the coupling between the orbital and spin angular momentum, the components L_z and S_z have no definite values. The spin-orbit interaction takes a state specified by the quantum numbers ℓ and s, and splits it into levels according to their j values: $j = \ell + s, ..., \left|\ell - s\right|$. If we have $\ell = 1$ and $s = 1/2$ in the absence of the spin-orbit interaction,
then j can takes two levels of 1/2 or 3/2 when the spin-orbit interaction is considered (Table 2.2).

Table 2.2 Spin, orbital and total quantum numbers for system with $\ell = 1$ and $s = 1/2$

$j = 3/2$			$j = 1/2$		
m_ℓ	m_s	m_j	m_ℓ	m_s	m_j
1	+1/2	+3/2	1	+1/2	
	-1/2	+1/2		-1/2	+1/2
0	+1/2	+1/2	0	+1/2	+1/2
	-1/2	-1/2		-1/2	-1/2
-1	+1/2	-1/2	-1	+1/2	-1/2
	-1/2	-3/2		-1/2	

Since the $m_j = 1/2$ state can arise from either an $m_\ell = 1$ and $m_s = -1/2$ state or an $m_\ell = 0$ and $m_s = 1/2$ state, the specifications of m_ℓ and m_s do not uniquely specify the energy, or to say it another way, the state with quantum numbers $|\ell, s, m_\ell, m_s\rangle = |1, 1/2, 1, -1/2\rangle$ has no definite energy. On the other hand, the state $|\ell, s, j, m_j\rangle$ does have a definite energy and is thus an eigenstate of the energy while $|\ell, s, m_\ell, m_s\rangle$ is not an eigenstate in the presence of the spin-orbit interaction. The various angular momenta are often represented in terms of a vector diagram.

From the diagram (Figure 2.2), we see that the projections of $\vec{L}$ and $\vec{S}$ on $\vec{J}$ have definite values. Thus, the vector diagram tells us that if we want to find the expectation value of the orbital angular momentum $\vec{L}$ along any direction in space, we project $\vec{L}$ on $\vec{J}$ and then project the resulting vector on the special direction of quantization z. Thus to calculate the expectation value of L_Z we find using the vector model:

$$\langle \ell, s, j, m_j \mid L_Z \mid \ell, s, j, m_j \rangle = \langle \ell, s, j, m_j \left| \frac{\vec{L} \cdot \vec{J}}{\left|\vec{J}\right|^2} (J_Z) \right| \ell, s, j, m_j \rangle \qquad (2.25)$$

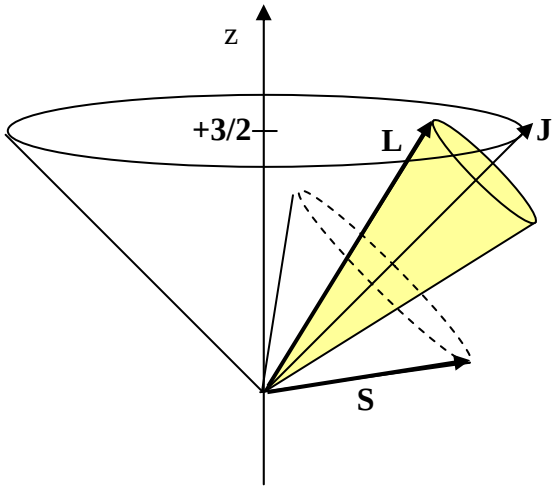

Figure 2.2 The diagram for $\ell = 5/2$, $s = 1/2$ and $m_j = 3/2$ shows that the total angular momentum $\vec{J}$ precesses around the z-axis. On the other hand, the angular momenta $\vec{S}$ and $\vec{L}$ precess around $\vec{J}$ [28]

The vector model is of great importance in considering the expectation value of vectors which are functions of the angular momentum. Thus by using the Eq. 2.4 in Eq. 2.2 the magnetic moment operator $\vec{\mu}_{Total}$ is

$$\vec{\mu}_{Total} = \frac{\beta_e}{\hbar}(g_L \vec{L} + g_S \vec{S}) \tag{2.26}$$

and the magnetic moment is directed along the vector $\vec{L} + 2\vec{S}$ (for $g_L = 1$ and $g_S = 2$). This magnetic moment vector is not along $\vec{J}$ and therefore has no definite value when projected on an arbitrary direction in space such as the z-axis (Figure 2.3). On the other hand, the projection of $\vec{\mu}_{Total}$ on $\vec{J}$ has a definite value. It is convenient to write Eq. 2.26 as

$$\vec{\mu}_{Total} = \frac{\beta_e}{\hbar} g\vec{J} \tag{2.27}$$

so that the energy of an electron in a magnetic field $\vec{B}$ is

$$E = -\vec{\mu}_{Total}.\vec{B} = -\beta_e (gBm_j) \tag{2.28}$$

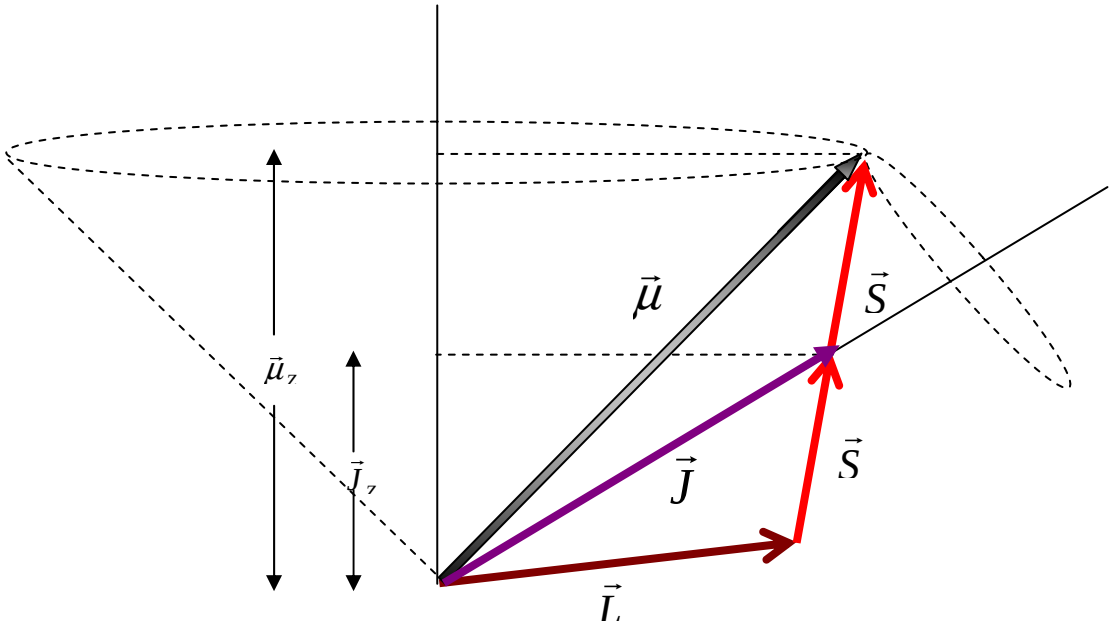

Figure 2.3 The vector model for the magnetic moment operator $\vec{\mu}$ [28]

where the Lande g-factor g represents the projection of $\vec{\mu}_{Total}$ on $\vec{J}$ so that

$$g = \left\langle \ell, s, j, m_j \left| \frac{(\vec{L} + 2\vec{S}) \cdot \vec{J}}{J^2} \right| \ell, s, j, m_j \right\rangle \tag{2.28}$$

To evaluate g we note that

$$(\vec{L} + 2\vec{S}) \cdot \vec{J} = (\vec{L} + 2\vec{S}) \cdot (\vec{L} + \vec{S}) = L^2 + 3\vec{L} \cdot \vec{S} + 2S^2 \tag{2.29}$$

by using Eq.2.23, we found the g value as

$$(\vec{L} + 2\vec{S}) \cdot \vec{J} = L^2 + \frac{3}{2}(J^2 - L^2 - S^2) + 2S^2 = \frac{3}{2}J^2 - \frac{1}{2}L^2 + \frac{1}{2}S^2 \tag{2.30}$$

We now take diagonal matrix elements of above equation in the $\left|\ell, s, j, m_j\right\rangle$ representation and find for the Lande g-factor as

$$g = \frac{\frac{3}{2} j(j+1) - \frac{1}{2}\ell(\ell+1) + \frac{1}{2} s(s+1)}{j(j+1)}. \tag{2.32}$$

2.2 Spin Hamiltonian

The most general form of the spin Hamiltonian contains a large number of terms, representing the Zeeman interaction of the magnetic electrons with an external field, level splittings due to indirect effects of the crystal field, hyperfine structure due to the presence of nuclear magnetic dipole and electric quadrupole moments in the central ion or ligands ions, and the Zeeman interaction of the nuclear moment with the external field. The effects of these terms on EPR spectrum depend on the physical system.

The interaction of electron with a static magnetic field is called as Electronic Zeeman interaction and can written in general form [29]

$$\mathrm{H}_{\mathrm{ze}} = \beta \vec{H} \cdot \vec{g} \cdot \vec{J} = \beta(H_x g_x J_x + H_y g_y J_y + H_z g_z J_z) \tag{2.33}$$

$$H_{ze} = \begin{vmatrix} \frac{5}{2}g_z H_z & \frac{\sqrt{5}}{2}(g_x H_x + i g_y H_y) & 0 & 0 & 0 & 0 \\ \frac{\sqrt{5}}{2}(g_x H_x - i g_y H_y) & \frac{3}{2}g_z H_z & \sqrt{2}(g_x H_x + i g_y H_y) & 0 & 0 & 0 \\ 0 & \sqrt{2}(g_x H_x - i g_y H_y) & \frac{1}{2}g_z H_z & \frac{3}{2}(g_x H_x + i g_y H_y) & 0 & 0 \\ 0 & 0 & \frac{3}{2}(g_x H_x - i g_y H_y) & -\frac{1}{2}g_z H_z & \sqrt{2}(g_x H_x + i g_y H_y) & 0 \\ 0 & 0 & 0 & \sqrt{2}(g_x H_x - i g_y H_y) & -\frac{3}{2}g_z H_z & \frac{\sqrt{5}}{2}(g_x H_x + i g_y H_y) \\ 0 & 0 & 0 & 0 & \frac{\sqrt{5}}{2}(g_x H_x - i g_y H_y) & -\frac{5}{2}g_z H_z \end{vmatrix}$$

here g is anisotropic in the system. The first and the second terms gives the off-diagonal elements in the (2J+1) × (2J+1) matrix. The last term gives only the diagonal terms.

The unpaired electrons have spin angular momentum S and orbital angular momentum L, total angular momentum J has possible values between |L-S| and L+S. This values can be called orbitally degenerate (2L+1) (Table 2.3), and this degeneracy is removed by the electric fields arising from ligands. The spin degeneracies (2S+1) are lifted by spin orbit coupling. The final degeneracy is determined by the local symmetry at the ion

Table2.3 Ground state properties of Free d^n Ions

Number of electrons n	S	L	J	Orbital degeneracy 2L+1	$^{2S+1}L_J$ L: 0 1 2 3 L: S P D F	Examples $3d^n$
1	1/2	2	3/2	5	$^2D_{3/2}$	Sc^{2+}
2	1	3	2	7	$^3F_2$	Cr^{4+}
3	3/2	3	3/2	7	$^4F_{3/2}$	Mn^{4+}
4	2	2	0	5	$^5D_0$	$Mn^{3+,}$ Fe^{4+}
5	5/2	0	5/2	1	$^6S_{5/2}$	$Mn^{2+,}$ Fe^{3+}
6	2	2	4	5	$^5D_4$	$Mn^{+,}$ Fe^{2+}
7	3/2	3	9/2	7	$^4F_{9/2}$	Fe^{+}
8	1	3	4	7	$^3F_4$	Fe^{0}
9	1/2	2	5/2	5	$^2D_{5/2}$	Ni^{+}

This local symmetry of ions and their hamiltonians can be explained by crystal field theory. Electrostatic potential energy of ion caused by its typical symmetric surroundings can be written in terms of spherical harmonics and it is simplified with “equivalent operators” by Stevens. The crystal field can be written in terms of equivalent operators O_k^q and their constants B_k^q. Sum of the equivalent operators listed below:

$$\mathrm{H_{cf}} = \sum B_k^q O_k^q \qquad (2.34)$$

$$O_2^0 = 3\mathrm{J}_z^2 - \mathrm{J}^2$$

$$O_2^2 = \frac{1}{2}(\mathrm{J}_+^2 - \mathrm{J}_-^2) \qquad (2.35)$$

$$O_4^0 = 35\mathrm{J}_z^4 - 30\mathrm{J}^2\mathrm{J}_z^2 + 25\mathrm{J}_z^2 - 6\mathrm{J}^2 + 3\mathrm{J}^4 .$$

For example; for a S=5/2, L=0,J=5/2, crystal field hamiltonian is

$$H_{cf} = \begin{vmatrix} 10B_2^0 + 60B_4^0 & 0 & \sqrt{10}B_2^2 & 0 & 0 & 0 \\ 0 & -2B_2^0 - 180B_4^0 & 0 & 3\sqrt{2}B_2^2 & 0 & 0 \\ \sqrt{10}B_2^2 & 0 & 8B_2^0 + 120B_4^0 & 0 & 3\sqrt{2}B_2^2 & 0 \\ 0 & 3\sqrt{2}B_2^2 & 0 & 8B_2^0 + 120B_4^0 & 0 & \sqrt{10}B_2^2 \\ 0 & 0 & 3\sqrt{2}B_2^2 & 0 & -2B_2^0 - 180B_4^0 & 0 \\ 0 & 0 & 0 & \sqrt{10}B_2^2 & 0 & 10B_2^0 + 60B_4^0 \end{vmatrix}$$

(2.36)

When the symmetry is less than cubic, fine structure term of the second degree will generally be present. This is an effect of more common occurrence than higher multipole fine structure, and hence we shall consider it separately, another reason for so doing that it occur in cases when g may be anisotropic. In terms of the spin operators O_2^0, O_2^2 mentioned above, the second degree or “quadrapole” terms are

$$B_2^0 O_2^0 + B_2^2 O_2^2 = B_2^0 \left\{3S_Z^2 - S(S+1)\right\} + \frac{1}{2} B_2^2 (S_+^2 - S_-^2) \qquad (2.37)$$

these may be expressed in an alternative form, which can be written as a single term $\vec{S} \cdot \vec{D} \cdot \vec{S}$, where $\vec{D}$ is a tensor quantity. Referred to the principal axes, this term is

$$D_X S_X^2 + D_Y S_Y^2 + D_Z S_Z^2 \qquad (2.38)$$

where it is convenient to take the sum of the there coefficients as zero, i.e. $D_X + D_Y + D_Z = 0$. If the sum is not zero, it can be made so by subtracting the quantity

$$\frac{1}{3}(D_X + D_Y + D_Z)(S_X^2 + S_Y^2 + S_Z^2) = \frac{1}{3}(D_X + D_Y + D_Z)S(S+1)$$

which is just a constant that moves all the levels up or down by the same amount, and so does not affect the resonance spectrum. The fact that one can set the sum of the three coefficients equal to zero means that there are really only two independent coefficients, as in Eq. 2.37.The connection between the two forms is revealed by manipulation of Eq. 2.38 as follows:

$$D_X S_X^2 + D_Y S_Y^2 + D_Z S_Z^2 = \frac{1}{2}(D_X + D_Y)(S_X^2 + S_Y^2) + \frac{1}{2}(D_X - D_Y)(S_X^2 - S_Y^2) + D_Z S_Z^2$$
$$= D\left\{S_Z^2 - \frac{1}{3}S(S+1)\right\} + E(S_X^2 - S_Y^2) \qquad (2.39)$$

where $D = \frac{3}{2}D_Z = 3B_2^0$, $\frac{1}{2}(D_X - D_Y) = E = B_2^2$. The form (2.38) is often convenient when all the coefficients are unequal, since the energy level can be computed for the case of a magnetic field along one axes, and the formulae for the other axes obtained bye cyclic permutation of the subscripts. The permutation required is (moving from column to column):

g_X	g_Y	g_Z
$\frac{3}{2}D_X = \frac{1}{2}(3E - D)$	$\frac{3}{2}D_Y = -\frac{1}{2}(3E + D)$	$\frac{3}{2}D_Z = D$
$\frac{1}{2}(D_Y - D_Z) = -\frac{1}{2}(D + E)$	$\frac{1}{2}(D_Z - D_X) = \frac{1}{2}(D - E)$	$\frac{1}{2}(D_X - D_Y) = E$

When axial symmetry is present, $D_X = D_Y$ and $E = 0$. The forms (2.37) and (2.39) are then to be prepared since they contain only one parameter. Even when $E \neq 0$, they have the advantage of containing only two parameters instead of there (which are not all independent). The quadrapole term have no effect on the energy of the doublet ($S = \frac{1}{2}$) but with larger values of S they produce a splitting of the levels when no magnetic field is present. For the case of $S = 1$ the energy levels can be expressed in a closed form when a magnetic field is applied, so long as it is parallel to one of the three principal axes of the tensor $\vec{D}$. The spin Hamiltonian, when an external field is applied along the z-axes, is

$$\mathrm{H} = g_Z \beta \vec{H} S_Z + D\left\{S_Z^2 - \frac{1}{3}S(S+1)\right\} + E(S_X^2 - S_Y^2) \qquad (2.40)$$

We haven't taken account into the interaction between nuclear moment and electronic moment spin hamiltonian so far. Given this, the splitted energy levels by Zeeman interaction again splitted which are smaller than fine structure. The interaction of magnetic moments of nucleus and electrons are very weak and called as hyperfine interaction. Their origin is rather complex, but essential principle can be understood in the following way. Consider a nuclear magnetic moment μ_{nuc} which sits in a magnetic field $\vec{B}_{elec}$ which is produced by ion and spin of all electrons. This produces an energy term $-\mu_{nuc}\vec{B}_{elec}$. Now $\vec{B}_{elec}$ is expected to be proportional to the angular momentum of all the electrons, $\vec{J}$, so that the hamiltonian for the hyperfine interaction can be written as

$$H_{Hf} = A\vec{I} \cdot \vec{J} \qquad (2.41)$$

Here $\vec{I}$ is the nuclear angular momentum and *A* is a parameter which can be determined from the experiment and measures the strength of the hyperfine interaction. So the total hamiltonian term is can be rewritten as,

$$\mathrm{H} = g_Z \beta \vec{H} S_Z + D\left\{S_Z^2 - \frac{1}{3}S(S+1)\right\} + E(S_X^2 - S_Y^2) + A(I \cdot S) \qquad (2.42)$$

and will be used to approach theoretically to the experimental EPR signals.

CHAPTER 3

OPERATING PRINCIPLE OF EPR

3.1 Introduction

Electron Paramagnetic Resonance, EPR, is a spectroscopic technique which detects species that have unpaired electrons. It is also often called Electron Spin Resonance (ESR). A surprisingly large number of materials have unpaired electrons. These include free radicals, many transition metal ions, and defects in materials. Free electrons are often short-lived, but still play crucial roles in many processes such as photosynthesis, oxidation, catalysis, and polymerization reactions. As a result EPR crosses several disciplines including: chemistry, physics, biology, materials science, medical science and many more.

The first observation of electron paramagnetic resonance peak was made in 1945 when Zavoisky detected a radio frequency absorption line from a $CuCl_2.2H_2O$ sample. Rapid development of electron paramagnetic resonance after 1946 was catalyzed by the widespread availability of complete microwave systems following World War II. One remarkable accomplishment in recent years has been the observation of an EPR signal from a single electron held in space by a configuration of applied electric and magnetic fields [30].

EPR is a magnetic resonance technique detects the transitions of unpaired electrons in an applied magnetic field. The electron has spin S=1/2, which gives it a magnetic property known as a magnetic moment. The magnetic moment makes the electron behave like a tiny bar magnet. When we supply an external magnetic field, the paramagnetic electrons can either orient in a parallel or antiparallel to direction of a

magnetic field. This creates two distinct energy levels for the unpaired electrons and allows us to measure them as they are driven between the two levels.

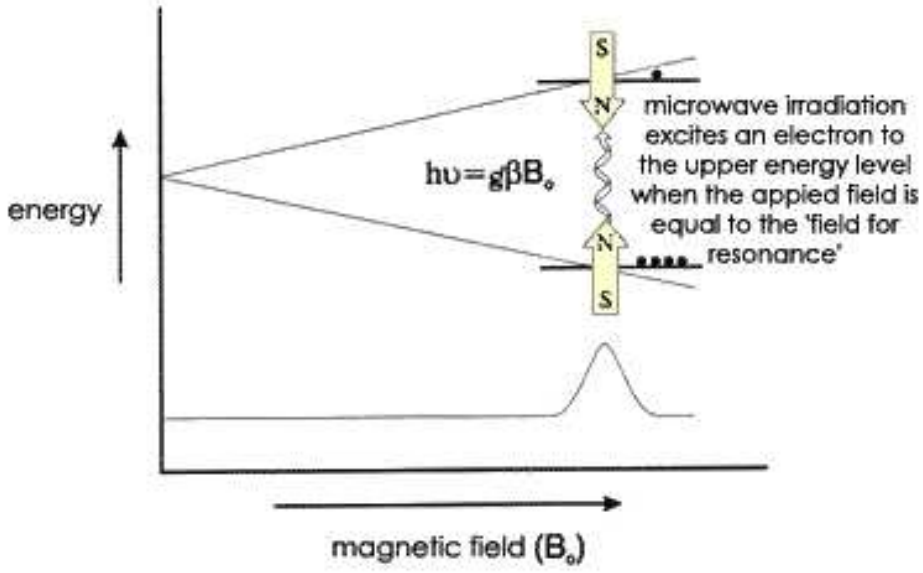

Figure 3.1 Energy levels for the unpaired electrons [30]

Initially, there will be more electrons in the lower energy level than in the upper level. We use a fixed frequency of microwave irradiation to excite some of the electrons in the lower energy level to the upper energy level. In order for the transition to occur we must also have the external magnetic field at a specific strength, such that the energy level separation between the lower and upper states is exactly matched by our microwave frequency. In order to achieve this condition, we sweep the external magnet's field while exposing the sample to a fixed frequency of microwave irradiation. The condition where the magnetic field and the microwave frequency are "just right" to produce an EPR resonance (or absorption) is known as the resonance condition and is described by the equation shown in the Figure 3.1.

$$E = h\nu \tag{3.1}$$

where h is Planck's constant and ν is the frequency of the radiation.

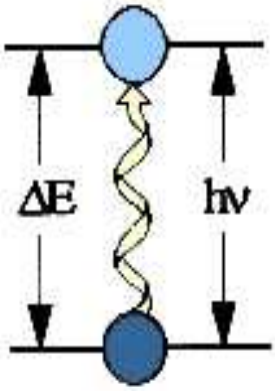

Figure 3.2 Transition associated with the absorption of electromagnetic energy [30]

The absorption of energy causes a transition from the lower energy state to the higher energy state. In conventional spectroscopy, is varied or swept and the frequencies at which absorption occurs correspond to the energy differences of the states. This record is called a spectrum. (Figure 3.3) Typically, the frequencies vary from the megahertz range for NMR (Nuclear Magnetic Resonance) (AM, FM, and TV transmissions use electromagnetic radiation at these frequencies), through visible light, to ultraviolet light. Radiation in the gigahertz range is used for EPR experiments.

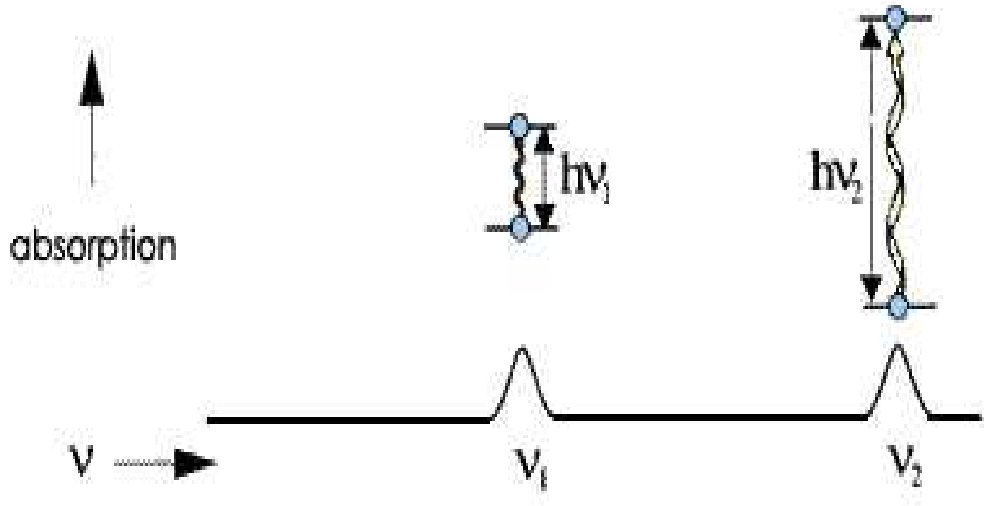

Figure 3.3 An absorption spectrum of different states [30]

The energy differences we study in EPR spectroscopy are predominately due to the interaction of unpaired electrons in the sample with a magnetic field produced by a magnet in the laboratory. This effect is called the Zeeman effect. Because the electron has a magnetic moment, it acts like a compass or a bar magnet when you place it in a magnetic field, B_0. It will have a state of lowest energy when the moment of the electron, μ, is aligned with the magnetic field and a state of highest energy when μ is aligned against the magnetic field. (See Figure 3.4) The two states are labeled by the projection of the electron spin, M_s, on the direction of the magnetic field. Because the electron is a spin ½ particle, the parallel state is designated as M_s = - ½ and the antiparallel state is M_s = + ½.

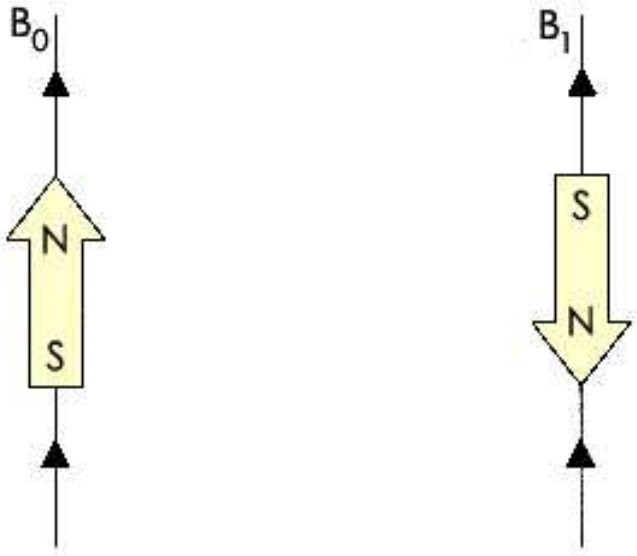

Figure 3.4 Minimum and maximum energy orientations of μ with respect to the magnetic field B_0 [30]

From quantum mechanics, we obtain the most basic equations of EPR:

$$E = g\mu_B B_0 M_S = \pm ½ g\mu_B B_0 \quad (3.2)$$

and

$$E = h\nu = g\mu_B B_0 \quad (3.3)$$

g is the g-factor, which is a proportionality constant approximately equal to 2 for most electrons, but which varies depending on the electronic configuration of the radical or ion. μ_B is the Bohr magneton, which is the natural unit of electronic magnetic moment.

Because we can change the energy differences between the two spin states by varying the magnetic field strength, we have an alternative means to obtain spectra. We could apply a constant magnetic field and scan the frequency of the electromagnetic radiation as in conventional spectroscopy. Alternatively, we could keep the electromagnetic radiation frequency constant and scan the magnetic field. A peak in the absorption will occur when the magnetic field tunes the two spin states so that their energy difference matches the energy of the radiation. This field is called the field for resonance. Owing to the limitations of microwave electronics, the latter method offers superior performance.

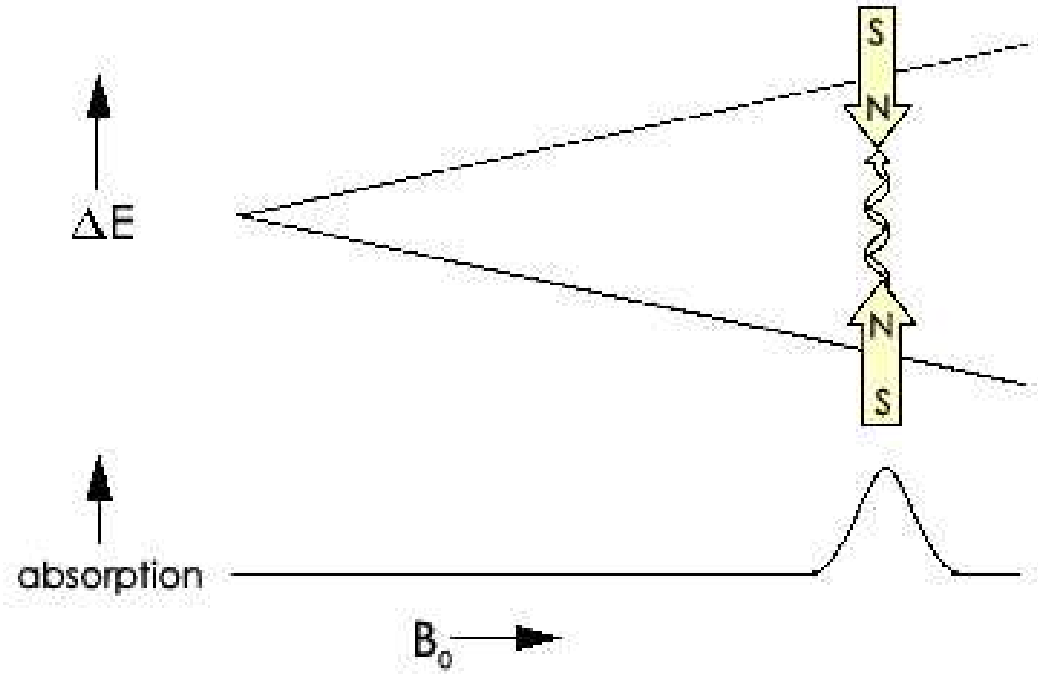

Figure 3.5 Variation of the spin state energies as a function of the applied magnetic field [30]

The field for resonance is not a unique fingerprint for identification of a compound because spectra can be acquired at several different frequencies. The g-factor,

$$g = h\nu / (\mu_B B_0) \quad (3.4)$$

being independent of the microwave frequency, is much better for that purpose. Notice that high values of g occur at low magnetic fields and vice versa. A list of fields for resonance for a g = 2 signal at microwave frequencies commonly available in EPR spectrometers is presented in Table 3.1:

Table 3.1 Field for resonance, B_{res}, for a g = 2 signal at selected microwave frequencies

Microwave Band	Frequency (GHz)	B_{res}(G)
L	1.1	392
S	3.0	1070
X	9.75	3480
Q	34.0	12000
W	94.0	34000

3.2 A Simple EPR spectrometer

The simplest possible spectrometer has three essential components: a source of electromagnetic radiation, a sample, and a detector. To acquire a spectrum, we change the frequency of the electromagnetic radiation and measure the amount of radiation which passes through the sample with a detector to observe the spectroscopic absorptions. Despite the apparent complexities of any spectrometer you may encounter, it can always be simplified to the block diagram shown in Figure 3.6.

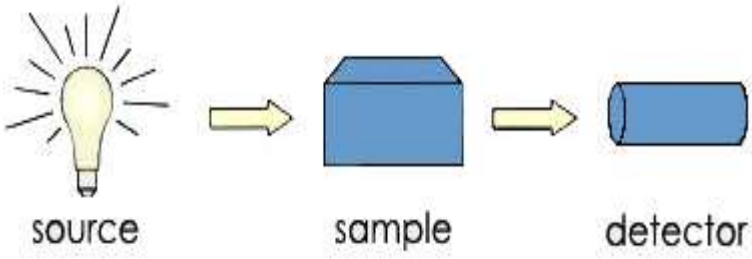

Figure 3.6 The simplest spectrometer [30]

Figure 3.7 shows the general layout of a Bruker EPR spectrometer. The electromagnetic radiation source and the detector are in a box called the microwave bridge. The sample is in a microwave cavity, which is a metal box that helps to amplify weak signals from the sample. As mentioned in the epr theory section, there is a magnet to tune the electronic energy levels. In addition, we have a console, which contains signal processing and control electronics and a computer. The computer is used for analyzing data as well as coordinating all the units for acquiring a spectrum.

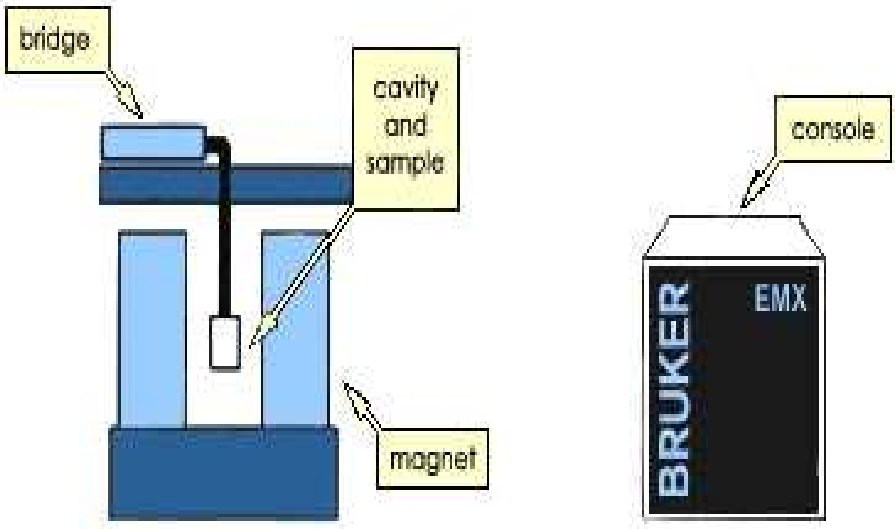

Figure 3.7 The general outlay of an EPR spectrometer [30]

3.3 EPR signal

The EPR experiment gives typical signals or splitted signals. Figure 3.8 shows how they work together to produce a spectrum.

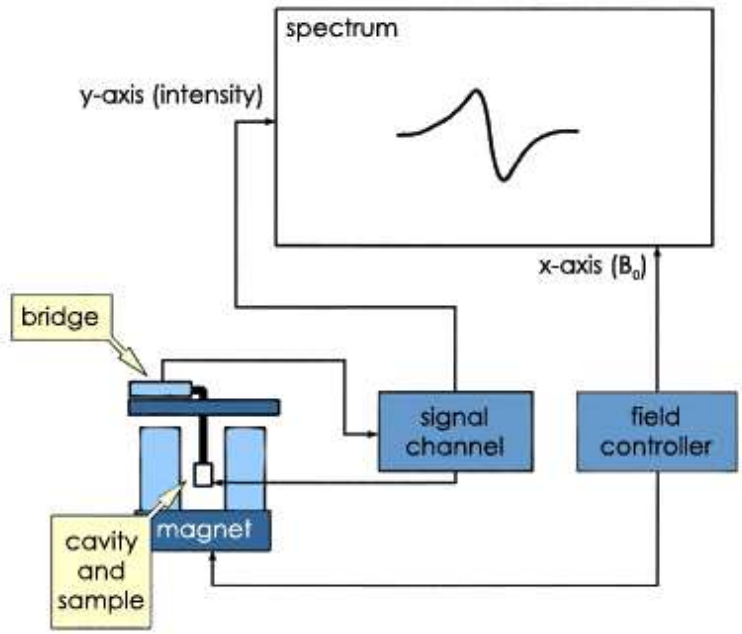

Figure 3.8 Block diagram of an EPR spectrometer [30]

3.4 Intensity of signals

The intensity of the EPR absorption is proportional to the concentration of the free radical or paramagnetic material present. Such as for free radical present, the method is extraordinarily sensitive, in favorable cases some 10^{-13} mol of free radical is detectable.

If we discuss the spectral line intensities in common there are three important factors to be considered: 1.The transition probability; the number of atoms or molecules initially in the state from which the transition occurs. 2. The population; the amount of material present giving rise to the spectrum. 3. The concentration or path length of sample.

1. *Transition probability*. The detailed calculation of the absolute transition probabilities is basically a straightforward matter, but as it involves, a knowledge of precise quantum mechanical wave functions of the two states between which the transition occurs, it can seldom be done with accuracy. However, it is often possible

to decide whether a particular transition is forbidden or allowed. This process is essentially the deduction of selection rules, which allow us to decide between which levels transitions will give rise to spectral lines, and it can often be carried out through pictorial arguments.

2. *Population of States.* If there are two energy levels from which transitions to a third are equally probable, then obviously the most intense spectral line will arise from the level which initially has the greater population. There is a simple statistical rule governing the population of a set of energy levels. For example, if we have a total of N molecules distributed between two different energy states, a lower and an upper with energies E_{lower} and E_{upper} respectively, we would intuitively expect most of the molecules to occupy the lower state. Proper statistical analysis bears this out and shows that, at equilibrium [31]

$$\frac{N_{upper}}{N_{lower}} = \exp(-\Delta E / kT) \qquad (3.5)$$

Where $\Delta E = E_{upper} - E_{lower}$, T is temperature in K, and *k* is a universal Boltzmann constant.

3. *Path length of sample.* For a sample which is absorbing energy from a beam of radiation, the more sample the beam traverses the more energy will be absorbed from it. It might be expected that twice as much sample would give twice the absorption, but a very simple argument shows that this is not so. Consider two identical samples of same material, S_1 and S_2, and assume that S_1 and S_2 alone absorb 50 percent of the energy falling on them, allowing the remaining 50 percent to pass through. If we pass a beam of initial intensity I_0 through S_1, 50 % of I_0 will be absorbed and the intensity of beam leaving S_1 will be ½ I_0; if we then pass this beam through S_2 a further 50 % will be absorbed, and 0.25 I_0 will leave the S_2. Thus two percent absorptions in succession do not add up to 100 percent but only to 75 percent absorption. An exact similar relationship exists between the concentration of a sample and the amount of energy absorption that is a doubling of the concentration produces something less than a doubling of the absorption. These relationships are best expressed in terms of Beer-Lambert law, which is;

$$\frac{I}{I_0} = \exp(-\varepsilon c l) \qquad (3.6)$$

where I_0 is the intensity of radiation falling on the sample, c and l are the sample concentration and length and ε is the extinction coefficient or absorption coefficient, which is a constant for a given type of transition (e.g. electronic, vibrational etc.) occurring within a particular sample. Clearly ε is closely connected with the transition probability discussed above, a large probability being associated with a large ε.

3.5 Linewidth of signals

The width of an EPR resonance depends on the relaxation time of the spin state under study. There are two possible relaxation processes, the spin-spin interaction is usually very efficient, unless the sample is extremely dilute, and gives a relaxation time of 10^{-6} - 10^{-8} s; the spin-lattice relaxation is efficient at room temperature (some 10^{-6} s) but becomes progressively less so at reduced temperatures, often becoming several minutes at the temperature of liquid nitrogen. For most samples the chosen typical relaxation time is 10^{-7} second, using this value in the Heisenberg uncertainty relation ($\delta\nu = 1$ MHz) will be mentioned below. A shorter relaxation time increases this width.

In general the width arises essentially because the energy levels of atomic and molecular systems are not precisely determined, but have a certain imprecision. Several factors contribute to this.

1. *Collision broadening.* Atoms or molecules in liquid and gaseous phases are in continual motion and collide frequently with each other. These collisions cause to some deformation of the particles and hence perturb, to some extent, the energies of at least the outer electrons in each. This immediately gives a possible explanation for the width of visible and ultra-violet spectral lines, since these deals largely with transitions between outer electronic shells. Equally vibrational and rotational spectra are broadened since collisions interfere with these motions too. In general,

molecular interactions are more severe in liquids than in gases and gas-phase spectra usually exhibit sharper lines than those of the corresponding liquid.

2. In the case of solids, the motions of particles are more limited in extent and less random in direction, so that solid-phase spectra are often sharp but show evidence of interactions by the splitting of lines into two or more components.

3. *Doppler broadening.* Again in liquids and gases the motion of the particles causes their absorption and emission frequencies to show a Doppler shift, since the motion is random in a given sample, shifts to both high and low frequencies occur and hence the spectral line is broadened. In general, for liquids collision broadening is the most important factor, whereas for gases, where collision broadening is less pronounced, the Doppler effect often determines the natural line width.

4. *Heisenberg uncertainty principle.* Even in an isolated, stationary molecule or atom the energy levels are not so sharp, due to the operation of a fundamental and very important principle, the Uncertainty Principle of Heisenberg. In effect it says that, if a system exists in an energy state for a limited time δt seconds, then the energy of that state will be uncertain to an extent δE where

$$\delta E \times \delta t \approx h/2\pi \approx 10^{-34}\, Js \qquad (3.7)$$

So we see that the lowest energy of state of a system is sharply defined since, left to itself, the system will remain that state for an infinite time; thus $\delta t = \infty$ and $\delta E = 0$. But, such as, the lifetime of an excited electronic state is usually only about 10^{-8} s, which gives a value for δE of about $10^{-34}/10^{-8} = 10^{-26}$ J. A transition between this state and the ground state will thus have an energy uncertainty of δE and a corresponding uncertainty in the associated radiation frequency of δE/h, which can be written as [31]:

$$\delta\nu = \frac{\delta E}{h} \approx \frac{h}{2\pi h \delta t} \approx \frac{1}{2\pi\delta t} \qquad (3.8)$$

3.5 Position of absorption; g factor

It is known that the spin energy levels of an electron are separated in an applied field B, by an amount:

$$\Delta E = g\beta B \tag{3.9}$$

where g is Lande splitting factor. A resonance absorption occur at a frequency, $\nu=\Delta E/h$ Hz from the Equation 3.9 we can see that the position of absorption varies directly with the applied field and since different EPR spectrometers operate at different fields, it is far more convenient to refer to the absorption in terms of its observed g value. So, rearranging Eq. 3.9

$$g = \frac{\Delta E}{\beta B} = \frac{h\nu}{\beta B} \tag{3.10}$$

and for example, resonance were observed at 8388.255 MHz in a field of 0.30 T, it would be reported as resonance at a *g* value of 2.0023 (for free electron). It is very remarkable fact that all free radicals and some ionic crystals have a g factor which varies only some ±0.003 from this value. The reason for this is essentially that in free radicals the electron can move about more or less freely over an orbital encompassing the whole molecule and it is not confined to a localized orbital between just two atoms in the molecule. In this sense it behaves in very much the same way as an electron in free space, having the L=0.

On the other hand, some ionic crystals have very different g factor values between about 0.2 and 8.0 having been reported. The difference here is that the unpaired electron is contributed by, and belongs to a particular atom in lattice, usually a transition metal ion. Thus the electron localizes in a particular orbital about the atom, and the orbital angular momentum (L value) couples coherently with the spin angular momentum giving rise to a value.

We said many ionic crystals show a g factor very close to the free electron value of 2, this may come out in two ways:

1. The ion contributing the electron may exist in an S state. For example, the ground state of Fe^{+3}, in which five *d* electrons are unpaired (S = 5/2, 2S+1=6) has zero orbital momentum. Thus L=0, J=S+L=S, and the term symbol is $^{6}S_{5/2}$. Since J=S, g=2

2. The electric fields set up by all the ions in a crystal may be sufficiently strong to uncouple the electrons orbital momentum from its spin momentum. Thus the value of L is immaterial and the g factor reverts to two. And, if the internal crystal field is weak, or if the paramagnetic electron is well shielded from the field (e.g. as in rare-earth metal, where the relevant electron orbit is buried deep within outer electron shells), L and S couple to produce a resultant J which itself precesses about the applied magnetic field. Intermediate cases also occur where L and S are only partly uncoupled, the residual orbital contribution to the energy giving rise to a *g* value not easily predictable theoretically.

CHAPTER 4

EXPERIMENTAL

4.1. Sample preparation

The synthesis of these solid solutions was carried out by the ceramic method from a stoichiometric mixture of corresponding starting components (oxides or carbonates). The mixture was thoroughly ground, pressed in pellets, and calcined at around 1600 K for 40 h and then at about 1800 K for 5 h. The optimal time of calcination was established by X-ray phase analysis and magnetic susceptibility measurements. These samples were synthesized by Mikhailova et all. and the details of the synthesis can be found in ref. 23. As an example; the solid solutions of $La_{1-0.25y}Sr_{1+0.25y}Mn_yAl_{(1-y)}O_4$ ($0.01 \leq y \leq 0.093$) have been prepared by solid state reaction from stoichiometric mixtures of La_2O_3, Mn_2O_3, Al_2O_3 and $SrCO_3$. All materials were purchased from Aldrich and had a purity of >99.9 %. The La_2O_3 and $SrCO_3$ were dried at 1120 K, before weighing, for more than 4 hrs. The starting materials were carefully homogenized by mechanical mixing and pressed into pellets. The calcination was carried out in a corundum crucible at 1773 K for 40 hours in air [23].

4.2. Magnetic Measurements

The EPR spectra have been recorded by a conventional X-band (ν=9.5-9.8 GHz) Bruker EMX model spectrometer employing an ac magnetic modulation technique. An Oxford continuous *He* gas flow cryostat has been used to cool the sample down to the measurement temperature while keeping the microwave cavity at ambient temperature during EPR measurements. The temperature was stabilized by a Lakeshore 340 temperature controller within an accuracy of 1 degree between 5 K and 300 K. The experimental data were stored into a computer for theoretical analysis.

CHAPTER 5

RESULTS AND DISCUSSIONS

5.1 Solid Solution of $LiMnO_2$-$LiGaO_2$, 2 mol % of Mn

Figure 5.1 shows the experimental X-band EPR spectrum and its simulation for $LiMnO_2$-$LiGaO_2$ in a magnetic field swept from 2.50 to 4.50 kG. The observed single peak has the characteristic properties for paramagnetic ion of Mn. The perfectly fitted simulation has Lorentzian line shape profile and proves that signal is centered at 3494 Gauss (*g* value is 2.003) with peak to peak line width of ΔH_{pp}=195 Gauss.

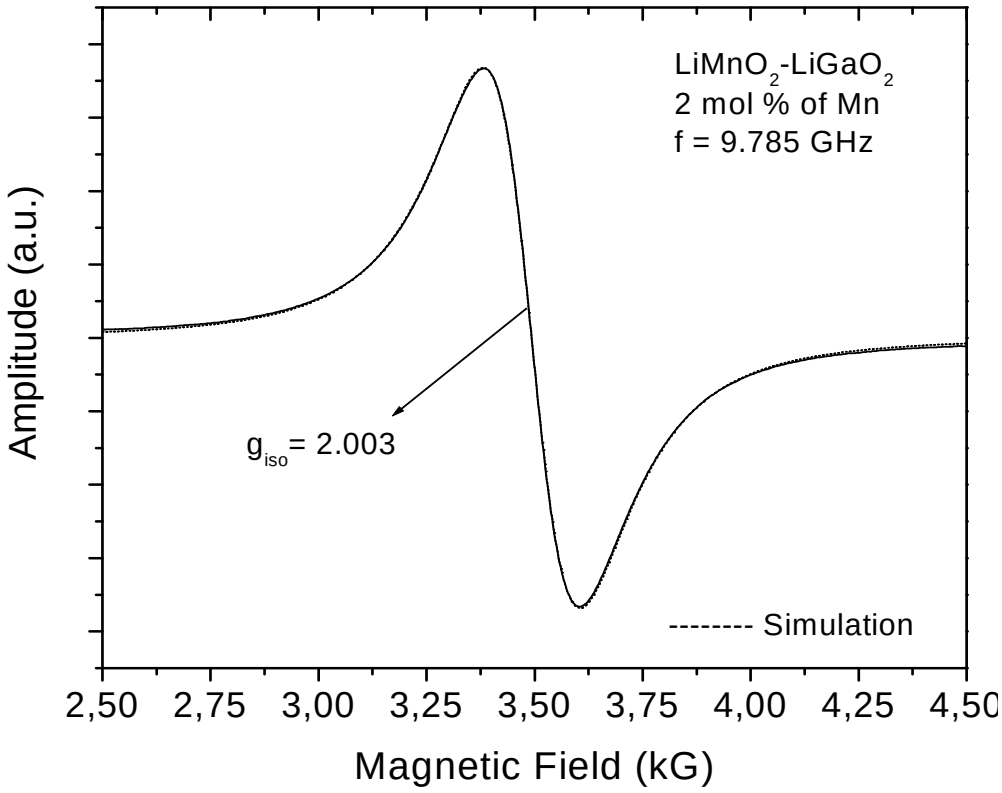

Figure 5.1 EPR spectrum of 2 mol % of Mn ions in $LiMnO_2$-$LiGaO_2$ solid solutions at room temperature

If the stoichiometric structure of $LiMnO_2$ is considered, the Mn^{3+} ions in the octahedral position [25] are expected to be paramagnetic source of signal. But, Mn^{3+} ion is known as EPR silent ion at X-band or at Q-band measurements [26]. However, the comparison of our results with literature investigations enables us that the signal originates from Mn^{2+} ions in the high spin state ($^6S_{5/2}$) and without any orbital magnetic moment contribution [34-36]]. The exactly symmetric line shape of curve can be attributed to the single type of species. Since the ^{55}Mn (100 % natural abundance) has a nuclear spin of I = 5/2, the six hyperfine signals are expected. In a study about the magnetic characterization of $LiMnO_2$, the short and long-range antiferromagnetic interactions are reported [32]. The long-range exchange interactions might be a reason for the lack of hyperfine structure. In addition, it is reasonable to think that Mn^{2+} ions have Mn^{2+} as nearest-neighbors.

The solid solution of $LiMnO_2$ exhibits very complex magnetic behavior with respect to temperature. So, the low temperature X-band EPR measurements should be reported as two different temperature intervals according to experimental results. In the first interval, from room temperature down to 30 K, the spectra were recorded in a magnetic field swept from 0 to 16.0 kG. The single peak without hyperfine lines maintains Lorentzian line shape characteristic with increasing absorption intensity as expected from a paramagnetic ion. The unexpected thing is that the increase of line width with decreasing temperature, ΔH_{pp}= 283 Gauss at 92 K. The increase in signal line width can not be explained by the exchange interactions between Mn^{2+} ions [34]. The Mn^{2+}- Mn^{2+} dipolar interactions are ascribed as one of the reasons for line broadening of resonance signal, in other words, the magnetic domain fluctuations increases with the decreasing temperature.

Below the 80 K some selected spectra with their simulations are shown in Figure 5.2. A very broad resonance peak without any hyperfine structure centered at about g = 2.00 appears and its peak to peak line width varies in a range from 5100 to 6330 Gauss for the given spectra in the figure with decreasing temperature. The line broadening continues also for narrow single peak, which originates from paramagnetic Mn^{2+} ions. Around 30 K, the narrow peak exactly disappears due to broadening and overlapping effects, instead we just observe a very broad absorption signal with maximum ΔH_{pp}= ~ 7350 Gauss. In the literature, the origin of very broad resonance signal is ascribed to the presence of paramagnetic Mn^{3+} and Mn^{4+} ions with electronic spin values of S = 2

and S = 3/2 respectively [33]. The lack of hyperfine features for broad and sharp peaks must be the exchange interactions between like and unlike ions, e.g. Mn^{2+}- Mn^{3+}, Mn^{2+}- Mn^{4+}, Mn^{3+}- Mn^{4+}. The dipolar interactions between unlike ions have contribution to broaden the EPR signals. The well fitted simulations have been obtained by the superposition of both broad and much narrower single peaks with the same Lande splitting factor, g = 2.00.

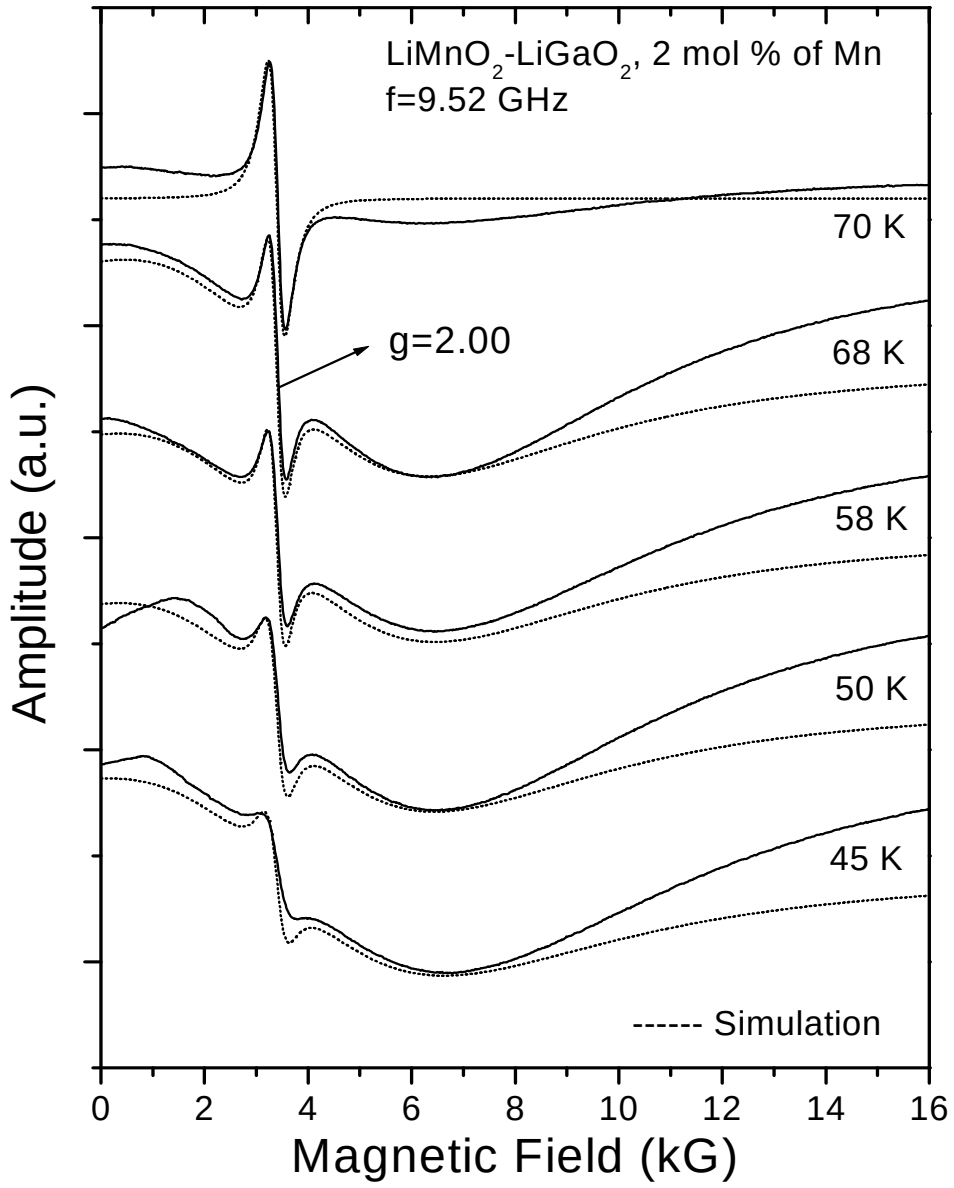

Figure 5.2 The temperature variation of EPR spectra of 2 mol % of Mn ions in $LiMnO_2$-$LiGaO_2$ solid solution below 80 K

The temperature variation of line width for narrow and broad peaks is shown in the Figure 5.3. The highest temperature value is 82 K to be able to specify the line width

of broad peak from experimental data and we observe the minimum value of peak to peak line width as 4950 Gauss. The line broadening rate increases sharply below 100 K for both peaks. However, we observe fluctuations in signal width of broad peak. This might be due to changes in heterovalent ion distribution (fluctuation, exchange of electrons among Mn ions with different ionic values) that is cluster formation or phase change in the temperature regime of compound. In the magnetic characterization study on orthorhombic $LiMnO_2$ compound performed by Jang *et al*. [32], in addition to the short and long-range of antiferromagnetic orderings, the spin glass behavior is reported as a result of geometrical frustration and magnetic disorder. The temperature dependence of line width and absorption intensity may clarify these cases for our $LiMnO_2$-$LiGaO_2$ solid solution.

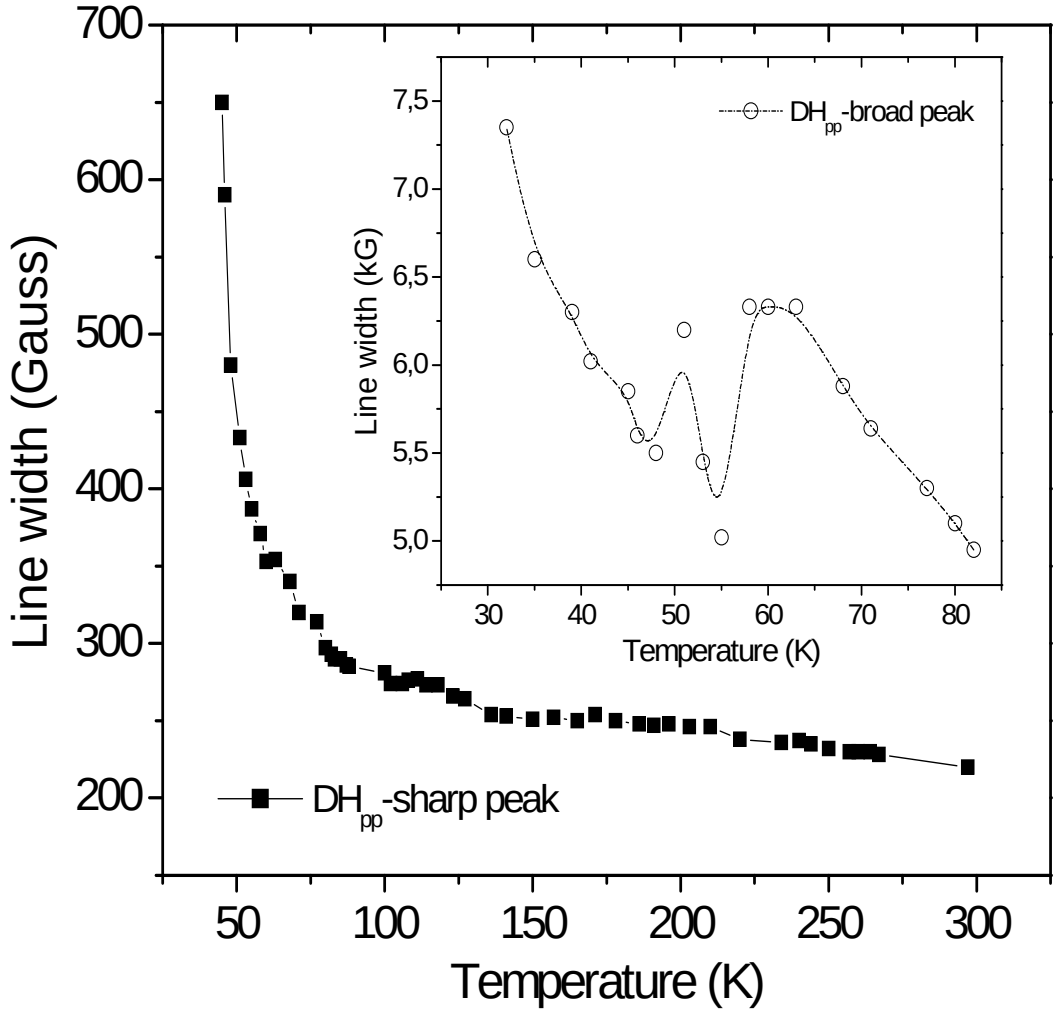

Figure 5.3 Temperature variation of line width for narrow and broad (as inset) peaks

The temperature dependence of absorption intensity and inverse absorption intensity for resonance signals are shown from 275 to 30 K in Figure 5.4a, from 30 to 5 K in Figure 5.4b. The absorption intensity of an EPR signal is proportional to the DC susceptibility of the studied sample [37] and it is well known that Mn has antiferromagnetic behavior under ~100 K [38].

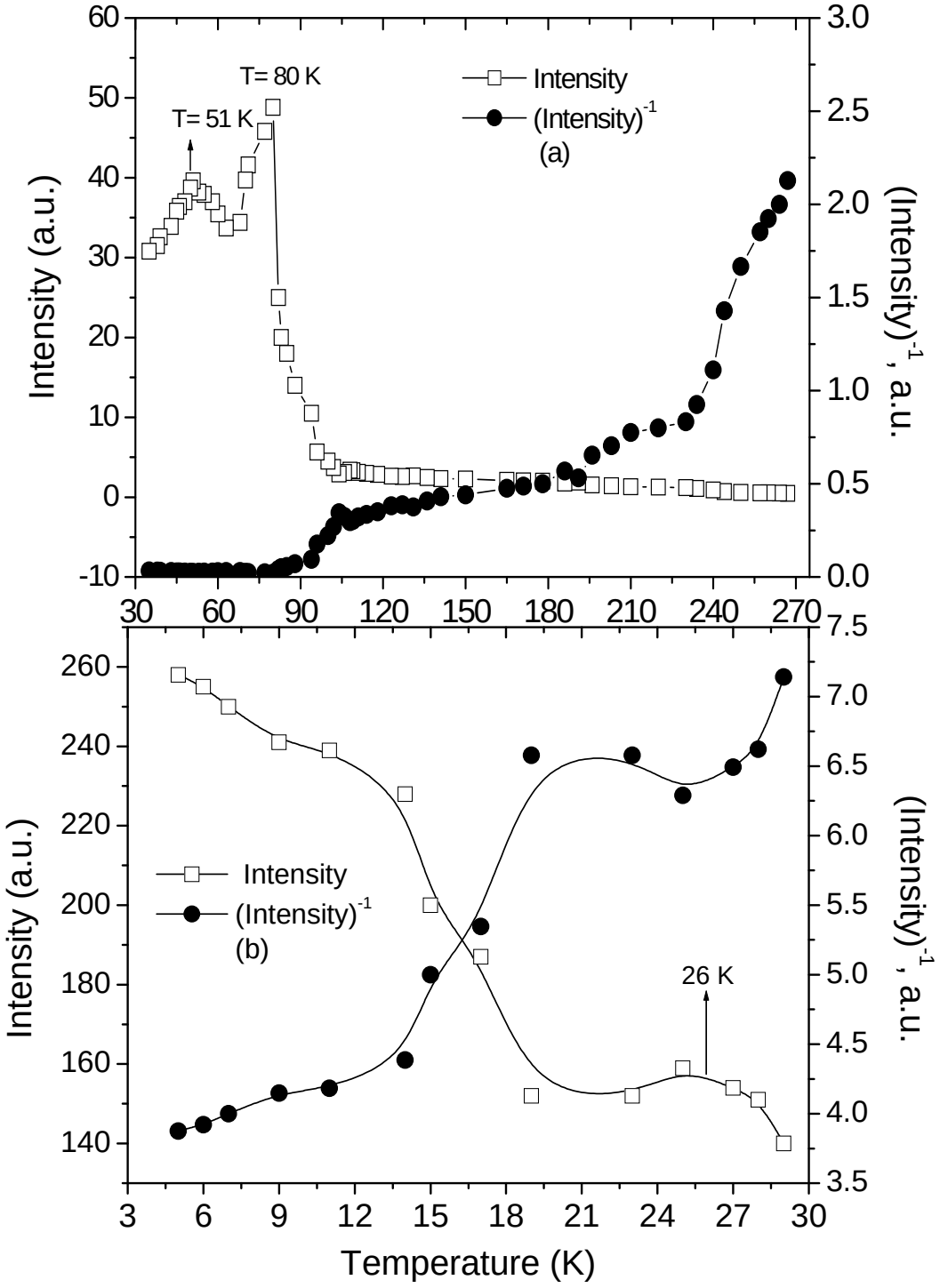

Figure 5.4 Temperature dependence of absorption intensity and inverse intensity are from 300 to 30 K in (a) and from 30 to 5 K in (b)

Here, an initial look at the Figure 5.2 might recall that it is difficult to obtain a 100 % reliable baseline correction and second integral calculations due out of range of resonance signal especially below 80 K. But the obtained trend was really consistent. So, the experimental observation exhibits two magnetic phase transitions around 80 and 51 K signed by arrow in Fig. 5.4a. The magnetic transitions are the evidence of valence increase of Mn, as the Mn valence increases the fraction of ferromagnetic couplings increases too. The partial substitution of Mn^{4+} ions for Mn^{3+} changes the character of dipolar and exchange interactions [39]. In the compounds, which contain the heterovalent ions of same element in the same geometry, the type of observed exchange interaction is called as Zener "double exchange" [40]. In this situation, an exchange event with an electron takes place between Mn^{4+} and Mn^{3+}cations separated by an O^{2-} anion, (Mn_1^{4+}– O^{2-} – Mn_2^{3+}). There are two origins of this electron transfer; (a) the transfer of a *p*-electron from Mn^{3+}cation to Mn^{4+}, and (b) a jump of a *d*-electron from second cation to its place. Since the spin of jumping electron in a state of lowest energy must be equally oriented in relation to S_1 and S_2, this effective indirect exchange has ferromagnetic character, $J_{Mn(IV)–Mn(III)} > 0$ [39]. In the temperature range of $100 < T < 230$ K, the magnetic susceptibility seems to fit well to usual Curie law and reflects an ideal paramagnetic behavior of localized Mn ions. Below 100 K and above 230 K, the temperature dependence of magnetic susceptibility obeys the Curie-Weiss law by corresponding to ferromagnetic and antiferromagnetic correlations. It is possible to say that another ferromagnetic interaction arises around 26 K from the Figure 5.4b.

Now we are able to compare the results reported by Jang *et al*. and our analyses that below 80 K, the sharp increase at the broadening rate of line width must arise not just due to dipolar interactions but also possibly with the contribution of spin disorder coming from the competition between ferromagnetic and antiferromagnetic interactions [41]. By considering the structural cluster formation (heterogeneity), magnetic fluctuation and the spin frustrations, there is enough reason to report spin glass like behavior for $LiMnO_2$-$LiGaO_2$ complex oxide.

5.2 Solid Solution of Ferrate, $LiFeO_2$-$LiGaO_2$, 5 mol % of Fe

Some experimental EPR spectra recorded from *$LiFeO_2$-$LiGaO_2$ (with 5 mol % of Fe)* at different temperature values are given in the Figure 5.5. Around room temperature a very strong resonance peak with $g \sim 2$ and ΔH_{pp}=103 Gauss line width and some minor peaks mainly in the low field region are observed. When temperature decreases a very sharp broadening at the line width of single resonance peak is observed while its amplitude decreases slightly. A remarkable broadening effect is not seen at the other minor peaks but some raisings at their amplitude with decreasing temperature. We are able to say that all observed resonance peaks exhibit isotropic resonance areas with decreasing temperature.

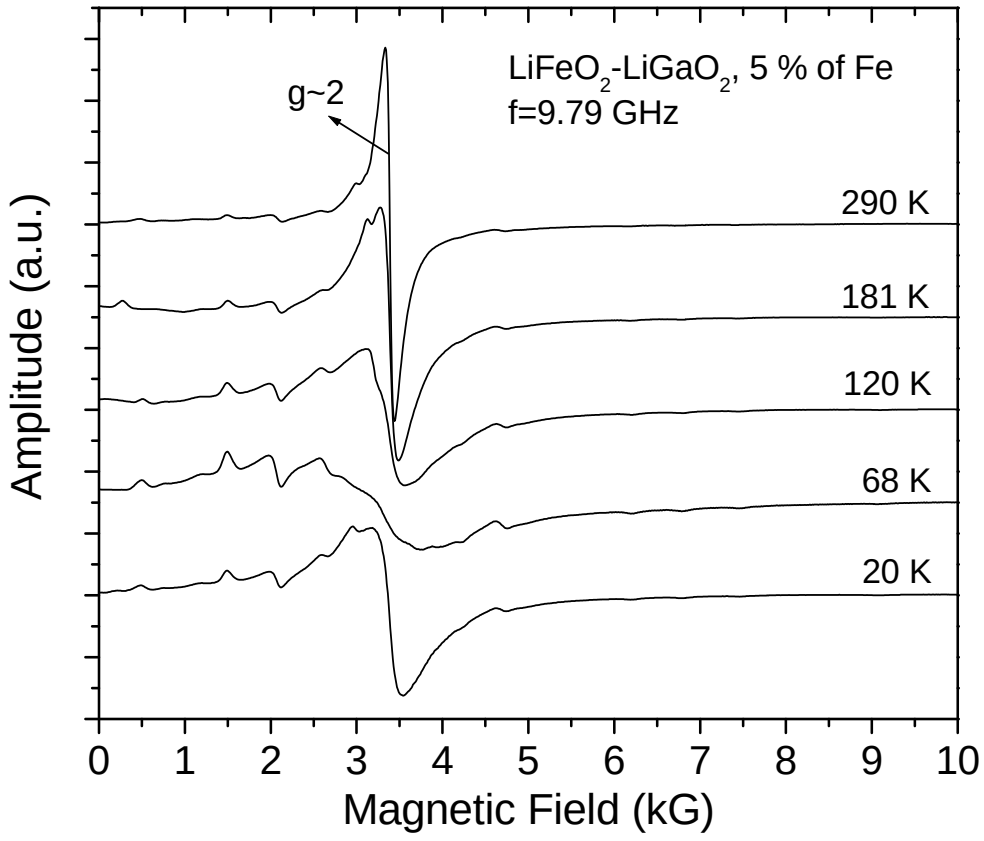

Figure 5.5 The temperature variation of EPR spectra of 5 mol % of Fe ions in $LiFeO_2$-$LiGaO_2$ solid solution below 110 K

According to stoichiometry of solid solution, Fe^{3+} ions with total electronic spin value of S=5/2 is expected to be as paramagnetic source. By using the SimFonia

package simulation program, we performed theoretical fit studies. Best fit parameters have been obtained by using the Hamiltonian given in the Eq.2.42 for the spectrum taken at 71 K as g = 2.24, A = 30 Gauss, D = 700 Gauss, E = 80 Gauss. So, we can say that there is reducing from cubic symmetry to orthorhombic and this position seems to be occupied mainly by the Fe^{3+} ions with nuclear spin value of I = 1/2. Orthorhombic structure for $LiFeO_2$ is also mentioned in the Ref. [1]. It is customary to define a parameter, $\lambda = E/D$ which takes values from 0 to 1/3, where $\lambda = 0$ means the symmetry is exactly axial and $\lambda = 1/3$ represents the maximum rhombic distortion, E= D/3, [42]. The rhombicity is equal to 0.114 for 71 K.

The temperature dependence of absorption intensity and inverse absorption intensity for resonance signals are shown from 300 to 7 K in Figure 5.6. We observe a very strong magnetic phase transition around 51 K. The deviation from almost paramagnetic behavior is observed between 25 to 80 K temperature interval and can be attributed to the ferromagnetic and antiferromagnetic interactions as it happens for 2 mol percent of Mn in the solid solution of $LiMnO_2$-$LiGaO_2$.

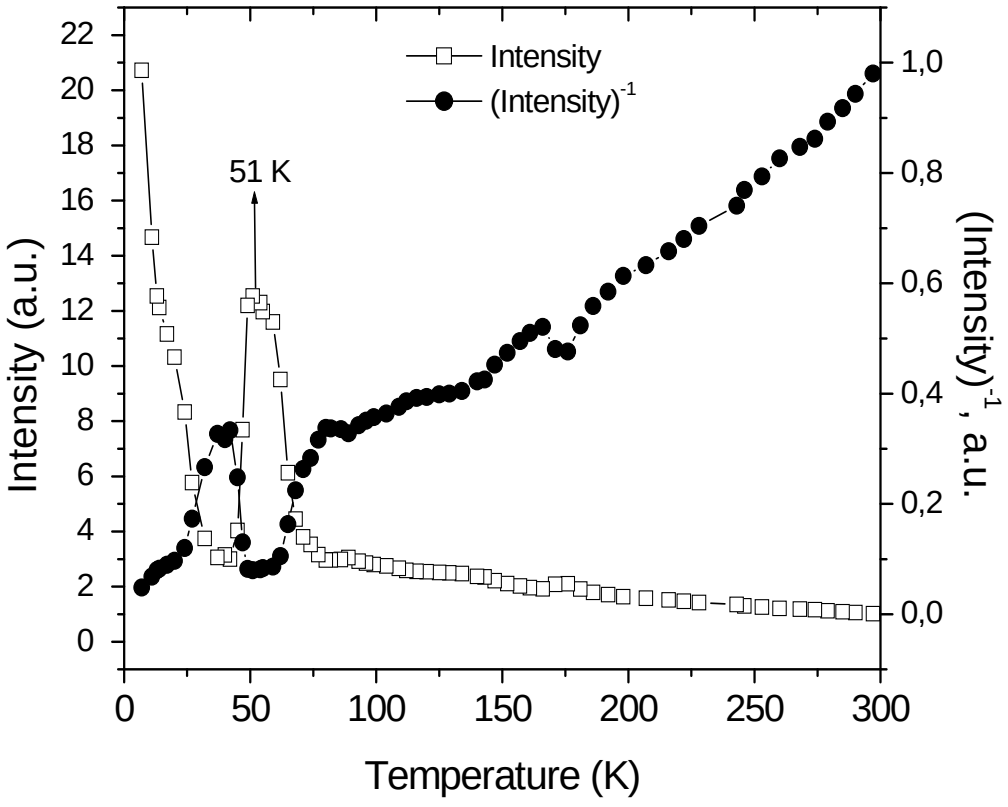

Figure 5.6 Temperature dependence of absorption intensity and inverse intensity are from 297 to 7 K

5.3 Solid Solution of Ferrate, $LiFeO_2$-$LiScO_2$, 5 mol % of Fe

Three experimental EPR spectra recorded from *$LiFeO_2$-$LiGaO_2$ (with 5 mol % of Fe)* at different temperature values are given in the Figure 5.7. Maximum resolution of the resonance peaks are observed at the spectrum recorded at 5 K. There are 6 well-resolved resonance peaks which are A, B, C, D, E and F with approximate Lande splitting values of g ~ 1.1, 1.52, 2.02, 3.3 5.3 and 21.2 respectively. Another peak around 8 kG comes from cavity below 30 K. Especially peaks A and E intensify with decreasing temperature. The peaks A, B and C exhibit a small amount of anisotropy with decreasing temperature. If we do simple comparison with peaks observed from *$LiFeO_2$-$LiGaO_2$*, except peak A, all other peaks with almost equal *g*-values were also recorded from *$LiFeO_2$-$LiGaO_2$*. By using the Hamiltonian equation for the spectrum recorded at 5 K, we determined the best-fit parameters as g = 2.27, A = 40 Gauss, D = 650 Gauss, E = 80 Gauss. The rhombicity is equal to 0.123 for 5 K. So, we can talk about paramagnetic source as Fe^{3+} ions in orthorhombic symmetry again consisted with the Ref. [7]

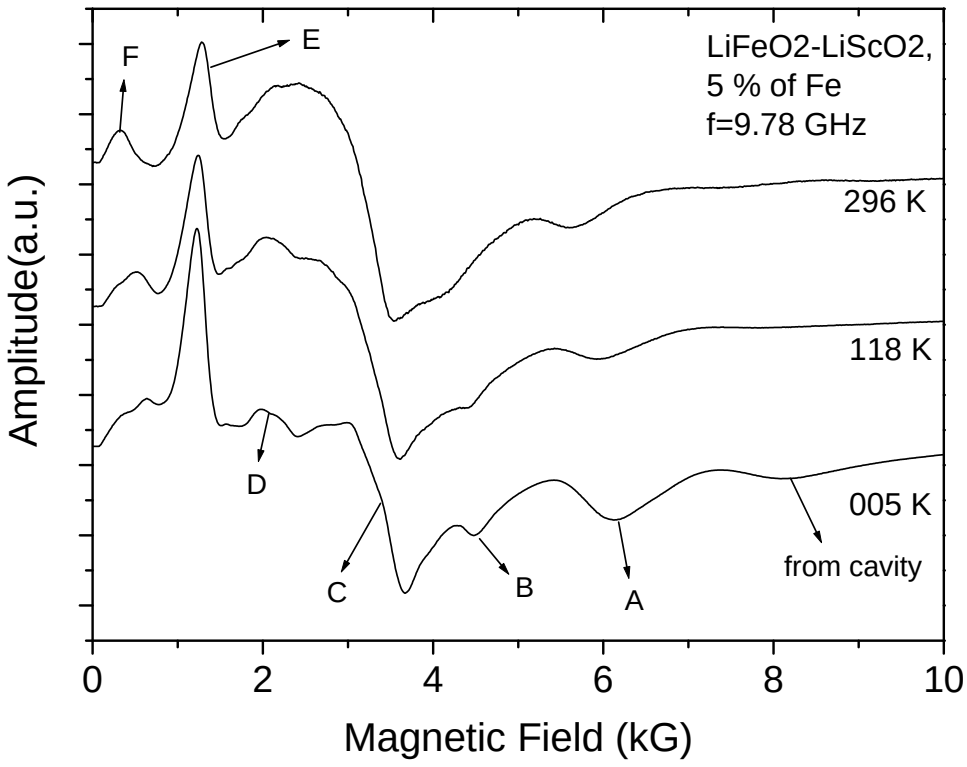

Figure 5.7 The temperature variation of EPR spectra of 5 mol % of Fe ions in $LiFeO_2$-$LiScO_2$ solid solution below 300 K

The temperature dependence of absorption intensity and inverse absorption intensity for resonance lines are shown in temperature interval of 5-300 K in Figure 5.8. We observe two magnetic phase transitions around 48 K and 95 K. The deflections from ideal paramagnetic that is Curie-Weiss type behaviors are observed above 230 K and below 100 K. The reason mainly seems to be ferromagnetic interactions for this compound.

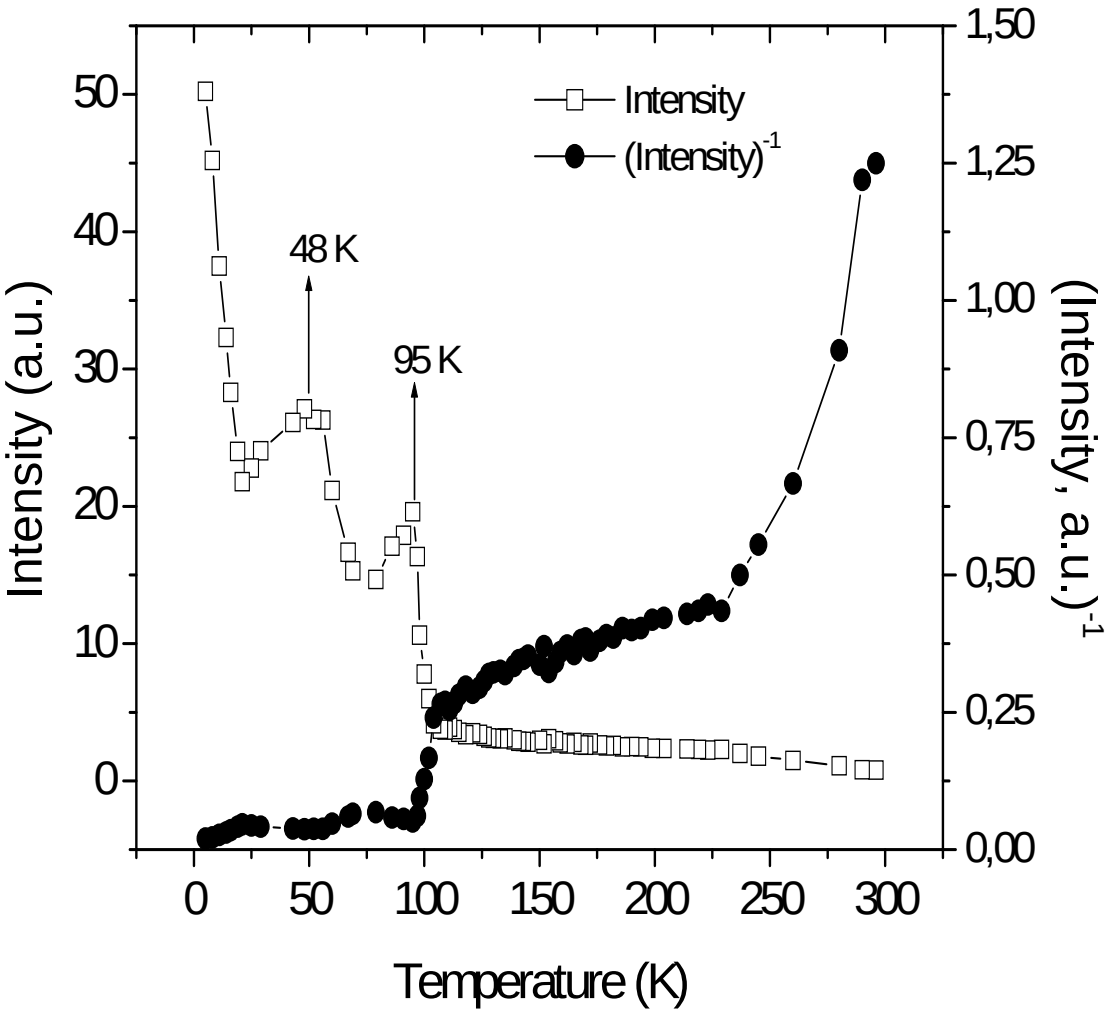

Figure 5.8 Temperature dependence of absorption intensity and inverse intensity are from 296 to 5 K

5.4 Solid Solution of $La_{0.75}Sr_{1.25}MnO_4$-$LaSrAlO_4$, 2 and 4 mol % of Mn

The EPR spectra registered at room temperature for 2 and 4 mol percent of Mn in $La_{0.75}Sr_{1.25}MnO_4$-$LaSrAlO_4$ solid solution are given in the Figure 5.9. Both spectra have two resonance peaks, one around 3485 Gauss with g = ~2 and the other very broad, unresolved shoulder like peak is around 1600 Gauss. The basic difference between two spectra is that the peak at g = ~2 includes hyperfine features in the spectrum recorded from the complex oxide including 2 mol % of Mn ion. Since the samples consist of powdered crystallites, the spectra for Mn ions are expected to contain absorption peaks splitted into 36 lines due to 6 electronic levels each of which is further split into six levels due to hyperfine interactions for any directions of an individual crystallite. Due to random orientation of the crystallites, these 36 absorption peaks overlap and give very broad curve as occurred in the figure. If the crystalline anisotropy very close to axial symmetry (slightly distorted into rhombic in this case) the spectral structure can seems to be in the figure. Especially, in the perpendicular part (originates from the crystallites with their symmetry axes oriented perpendicularly to the external field), the peak separation exhibits very strong anisotropy.

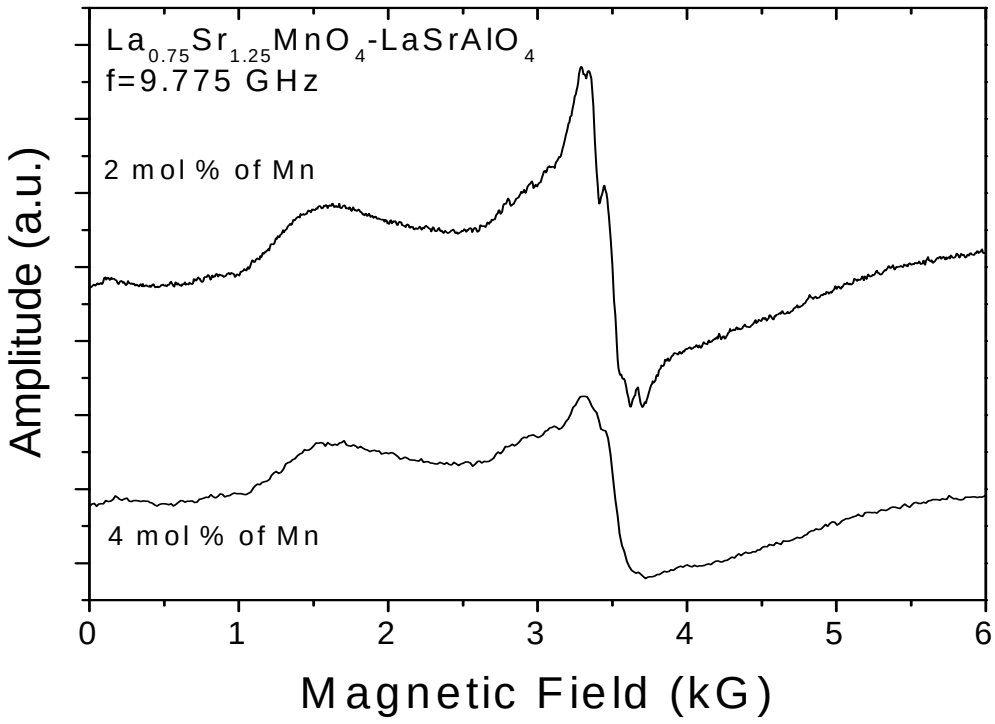

Figure 5.9 Experimental EPR spectra of 2 mol % and 4 mol % of Mn in $La_{0.75}Sr_{1.25}MnO_4$- $LaSrAlO_4$ solid solution at room temperature

In the literature, $La_{0.75}Sr_{1.25}MnO_4$ compound contains heterovalent manganese ions of Mn^{3+} and Mn^{4+} as paramagnetic sources [31]. The analyses of resonance peak around the g = ~2 recorded from $LiMnO_2$ offers that Mn^{2+} is another probable paramagnetic source. If we consider the nonstoichiometric structure of polycrystalline sample, the probability of this case is difficult to predict. So a detailed analysis can illuminate us about the source of these two resonance lines. By this purpose, the two spectra taken at 159 K and 7 K temperature values with their simulations are given in the Figure 5.10. The significant changes were observed at the spectrum registered at 7 K that is two additional peaks; peak A and B located around 0.85 kG and 6 kG respectively are observed with decreasing temperature. Peak A arises below 120 K while peak B below 14 K. The signal around g = ~2 maintains its hyperfine feature at every recorded temperature value.

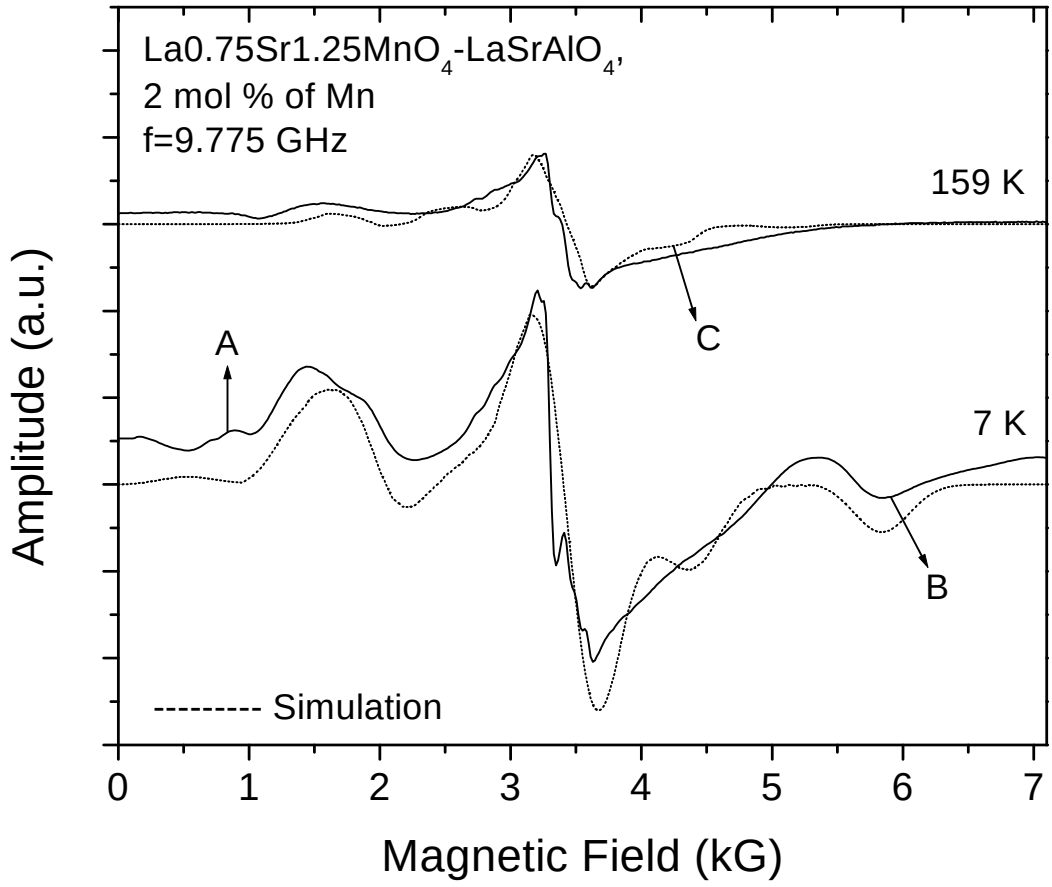

Figure 5.10 The EPR spectra of 2 mol % of Mn in $La_{0.75}Sr_{1.25}MnO_4$-$LaSrAlO_4$ solid solution registered for two different temperature values below room temperature

Best fit parameters have been obtained by using SimFonia simulation program and Hamilton equation for the spectrum taken at 159 K as g = 2.00, A = 70 Gauss, D = 440 Gauss, E = 130 Gauss and S = 5/2, while these parameters were equal to g = 2.00, A = 60 Gauss, D = 500 Gauss, E = 120 Gauss and S = 5/2 for the spectra taken at 7 K. So the axially distorted octahedral position seems to be occupied mainly by the Mn^{2+} ions with electronic spin value of S = 5/2. The rhombicity is equal to λ = 0.295 and 0.240 at 159 and 7 K values, respectively. The simulated spectrum includes another peak, C that is not separable due to overlapping and broadening effects at the negative side of broad experimental signal at high temperatures.

Figure 5.11 shows a closer examination and simulation for the hyperfine structure of the peak centered around 3485 Gauss in a magnetic field swept from 2.20 to 4.20 kG at room temperature again.

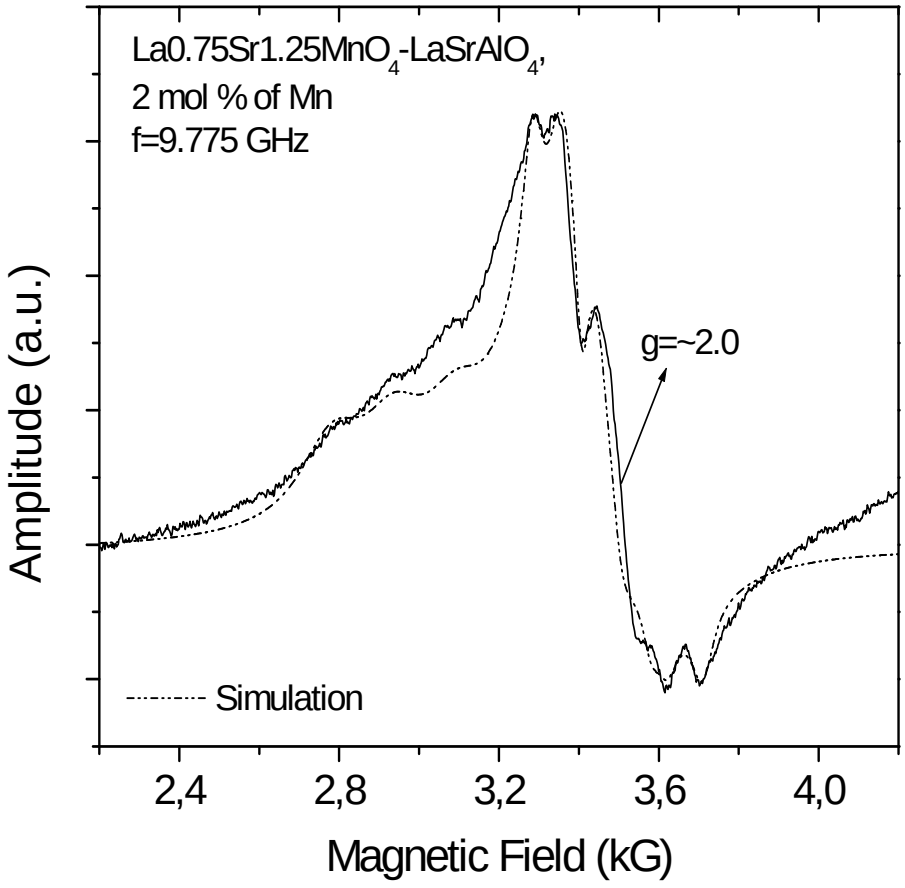

Figure 5.11 EPR spectrum for hyperfine structure resolution for 2 mol % of Mn ions in $La_{0.75}Sr_{1.25}MnO_4$-$LaSrAlO_4$ solid solution at room temperature

The positions of allowed hyperfine transitions are expressed by the angular dependent equations in the Ref. [43]. A home made program has been written to simulate the theoretical spectrum. The great accordance with experimental one has been obtained by using the fit parameters of g = 2.01, A = 107 Gauss, D = 490 Gauss, E =145 Gauss and S = 5/2. The rhombicity is equal to $\lambda = 0.296$ at room temperature and nearly equal to parameter obtained for the spectrum taken at 159 K by using the SimFonia program.

So, by using literature investigations [33, 44] and theoretical fit studies on the spectra, we are able to say that at different temperature values Mn^{2+} ions are assigned into rhombic symmetry. Mn^{2+} is a $3d^5$ ion with electronic spin of S = 5/2, it is known that d^5 metal ions under crystal field stronger than Zeeman field gives rise to three Kramers doublets $|\pm 5/2\rangle$, $|\pm 3/2\rangle$ and $|\pm 1/2\rangle$ in the case of axially distorted octahedral symmetry. An application of Zeeman field splits the spin degeneracy of the Kramers doublets and resonances are observed due transitions with in the Kramers doublets [36]. Chakradhar *et al*. signs that shoulder like peak arises from the transitions between energy levels of middle Kramers doublet $|\pm 3/2\rangle$ and the other peak correspond to the lower $|\pm 1/2\rangle$ doublet as the magnetic source of Mn^{2+} ions. But in the study performed by Ramirez-Rosales *et al*. [42], there are three observed transition peaks from Mn^{2+} ions due to strong crystalline field. In the study, the broad shoulder at g = ~ 4.3 correspond to the transition between energy levels of (–5/2 ↔ –3/2; –3/2 ↔ –1/2), the second resonance peak centered at g = ~2 correspond to the lower Kramers doublet, 1/2 ↔ –1/2. The third one is another shoulder like resonance signal arises at around 5495 Gauss for X-band measurements corresponding to transitions between -1/2 ↔ –3/2, all three are allowed ΔM_S=1 transitions. This third peak (peak B) had appeared in our experimental X-band spectra at the measurements performed under 14 K.

Below room temperature, some additional spectra recorded for 2 mol % of Mn ions in $La_{0.75}Sr_{1.25}MnO_4$-$LaSrAlO_4$ solid solution are shown in Figure 5.12. The peak B intensifies drastically below 14 K. This might be due changing amount of contribution from Mn^{2+} ions that occupy the octahedral position in the resonance region centered at g = ~2. If we reconsider the very broad and intensive structure of the observed peak, especially its negative side is wider and more intense; this case seems to be true at every

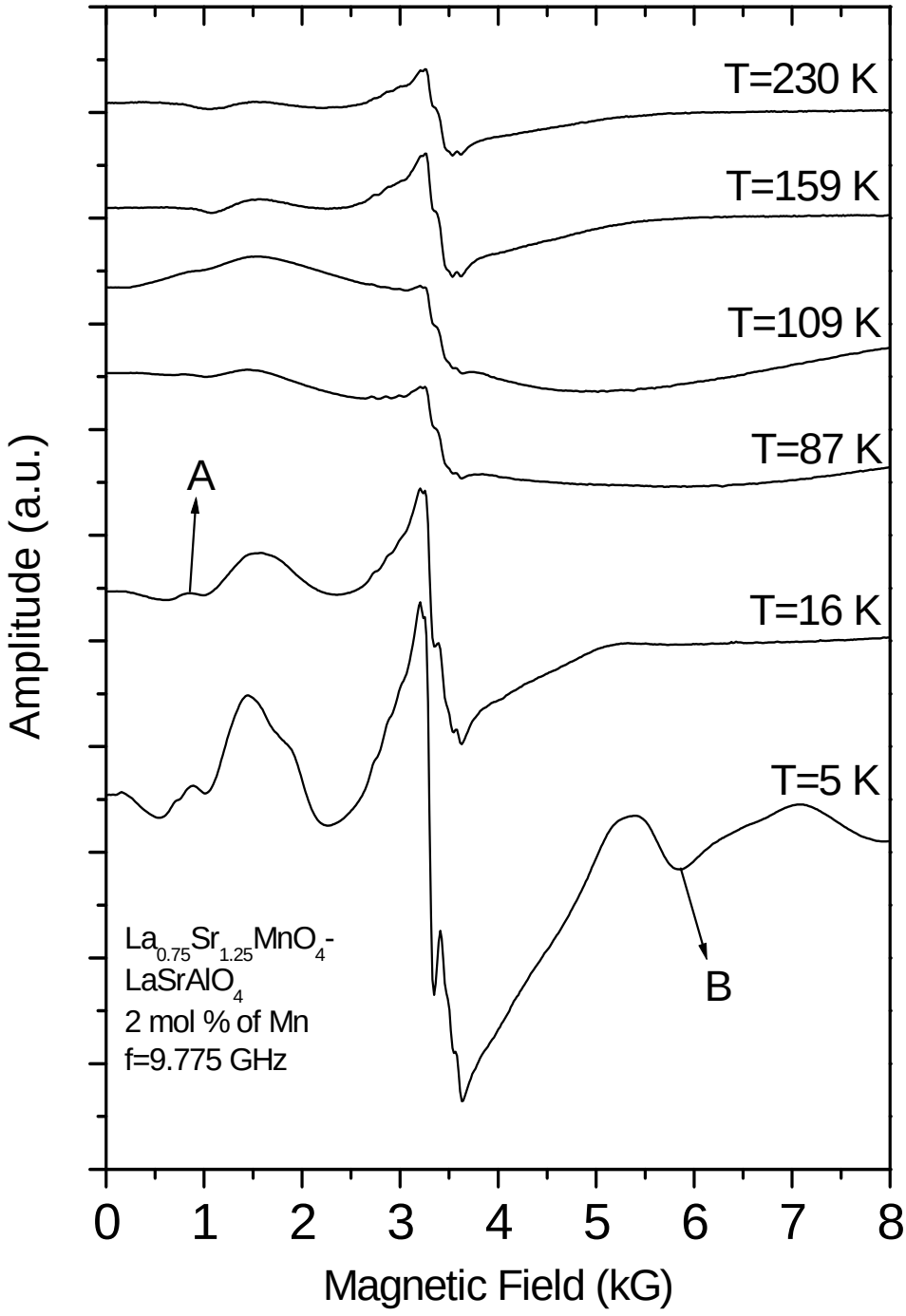

Figure 5.12 The temperature variation of EPR spectra of 2 mol % of Mn in $La_{0.75}Sr_{1.25}MnO_4$-$LaSrAlO_4$ solid solution below room temperature

value of temperature. Another fact that the g = ~2 resonance is more intense than the other resonance signals as whole. This observation indicates that more amounts of Mn ions are present in the octahedral environment than in the rhombic environment. The presence of peak B also enables us to determine the corresponding transitions between

energy levels as the same expressed by Ramirez-Rosales *et al*. The other rising peak with decreasing temperature, peak *A* in the low field region is ascribed to the forbidden $\Delta M_S=2$ transitions originate from the Mn^{4+} ion in the Ref. [33]. The reason for increasing intensity of forbidden transitions is given as the increase at spin-lattice (T_1) and spin-spin (T_2) relaxation times with decreasing temperature by Rakhimov *et al*. again. The exchange and dipolar interactions between Mn^{2+}, Mn^{3+} and Mn^{4+} ions are observed strongly in the temperature range of 30-110 K and cause to large broadening effects on the spectra.

We did not observe any peak that originates directly from Mn^{3+} ion at any temperature range consistently with the literature. The similar characteristics with respect to temperature are observed for 4 mol % of Mn ions without any significant change. As the 2 mol % Mn ion concentration increases to 4 mol %, the resolution of HFS sextet exactly disappears leaving behind a single broad line due to ligand field fluctuations in the Mn^{4+} ion vicinity and also due to dipolar interactions [36].

The temperature dependence of absorption intensity and inverse absorption intensity for 2 and 4 mol % of Mn in $La_{0.75}Sr_{1.25}MnO_4$-$LaSrAlO_4$ solid solution are given in the Figure 5.13a and 5.13b respectively. We observe two remarkable magnetic phase transitions around 67 K and 105 K for two different concentrations of Mn. The transition intensity around 105 K seems to be little bit more for 2 mol % of Mn while transition around 67 K is stronger for 4 mol of Mn. The deviations from ideal paramagnetic behavior can be attributed to the ferromagnetic and antiferromagnetic interactions as it happens for 2 mol percent of Mn in the solid solution of $LiMnO_2$-$LiGaO_2$.

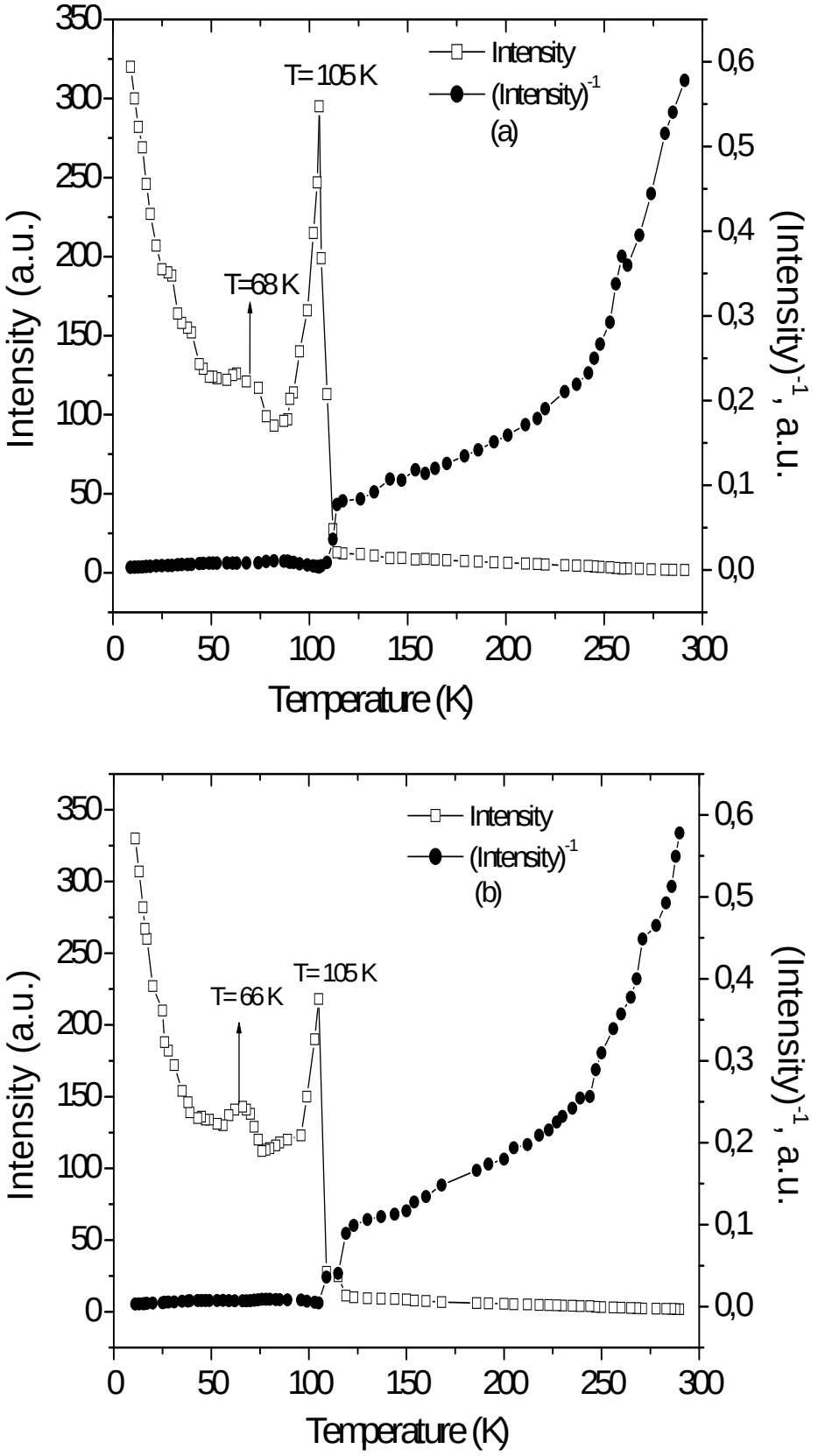

Figure 5.13 Temperature dependence of absorption intensity and inverse intensity for (a) 2 mol % of Mn and (b) 4 mol % of Mn

5.5 Solid Solution of Ferrate, $LaFeO_3$-$LaGaO_3$, 3 mol % of Fe

A simulation and the three experimental EPR spectra recorded from solid solution of *$LaFeO_3$-$LaGaO_3$* in perovskite structure are given in the Figure 5.14. At the spectrum recorded in room temperature, there are well-separated 6 resonance lines. In real we can categorize these peaks into 3 different paramagnetic centers. The first group consists of 3 lines with g values of g_1 = 1.87, g_2 = 2.07, g_3 = 2.5. The second group consists of 2 lines of g_4 = 4.4 and g_5 = 8.26 values. The other peak with g_6 = 10. When the temperature decreases, the three more resonance peaks occur in the high magnetic field region with g_7 = 1.37, g_8 = 1.19 and g_9 = 0.93 values.

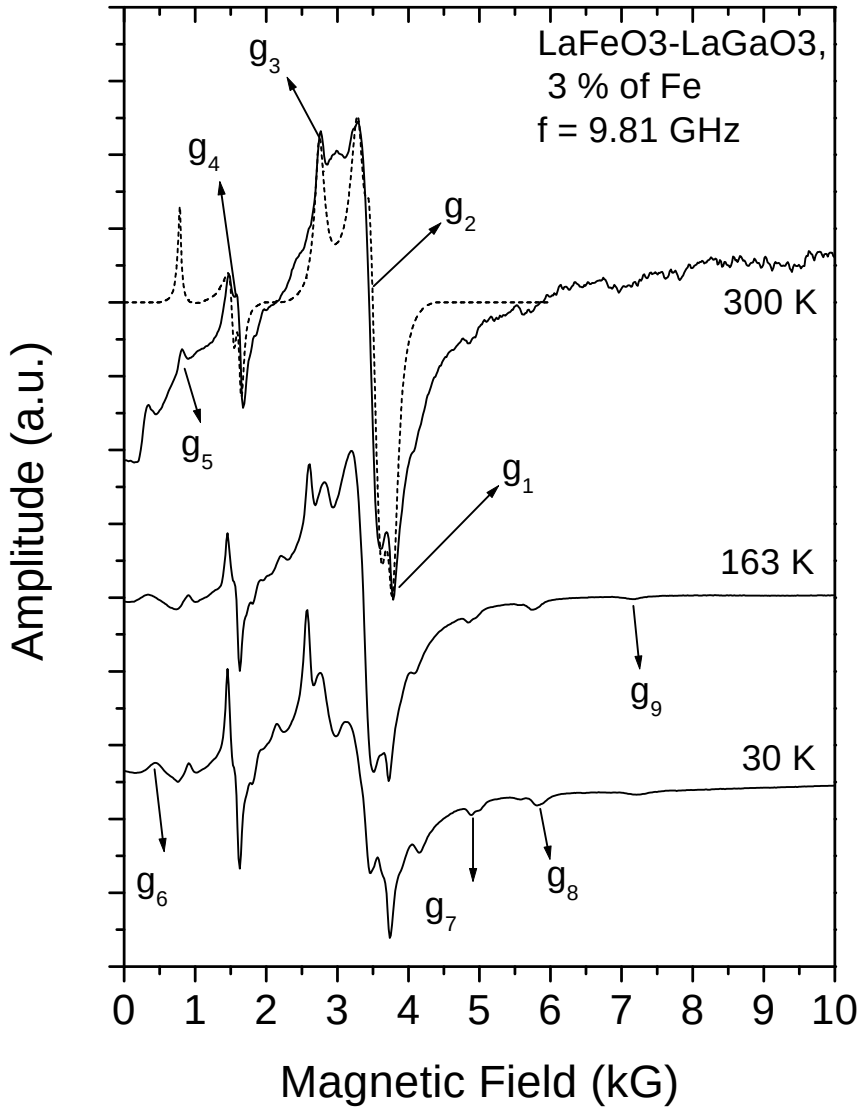

Figure 5.14 The temperature variation of EPR spectra of 3 mol % of Fe ions in $LaFeO_3$-$LaGaO_3$ below 300 K

All observed peaks exhibit isotropic behavior with decreasing temperature. The origin of the first group is given as Fe^{3+} ions (with *g* values ~2) in oxidic clusters in the references [45-47]. This result is in accordance with the cases reported by T. Seiyama et al [13]. When we compare the line width of resonance peaks around g~2 with a very broad resonance peak registered by A.Tavman et al [47], it is possible to say that polycrystalline ordering is the major case than clustering.

As the paramagnetic source of second group, the theoretical simulation and literature investigation studies show that the signal having the $g_4 = g_\perp = 4.4$ value is the well-pronounced perpendicular component and the shoulder with $g_5 = g_\parallel = 8.26$ value is the parallel component of paramagnetic peak arising from the Fe^{3+} ion possessing penta or hexa coordinated with rhombic crystal field [48-50]. In some cases a parallel resonance component near $g_\parallel = 6.0$ are reported having well resolved shoulders around $g_\perp = 4.2$ [48, 51]. No such signal is observed in our recorded spectra. When Fe^{3+} ions are located in a crystal field environment, the ^6S ground state splits into three Kramer doublets $|\pm 1/2\rangle$, $|\pm 3/2\rangle$ and $|\pm 5/2\rangle$. The resonance peak with $g = g_\perp = 4.4$ arises from $|\pm 3/2\rangle$ doublet [52]. The origin of all other peaks is given as Fe^{3+} ions in the study performed by T. Castner et al [53].

The temperature dependence of absorption intensity and inverse absorption intensity for 3 mol % of Fe in $LaFeO_3$-$LaGaO_3$ solid solution are given in the Figure 5.15. We observe a magnetic phase transition region between 25 K and 100 K especially around 98 K. The deviation from ideal paramagnetic behavior can be attributed to the ferromagnetic interactions.

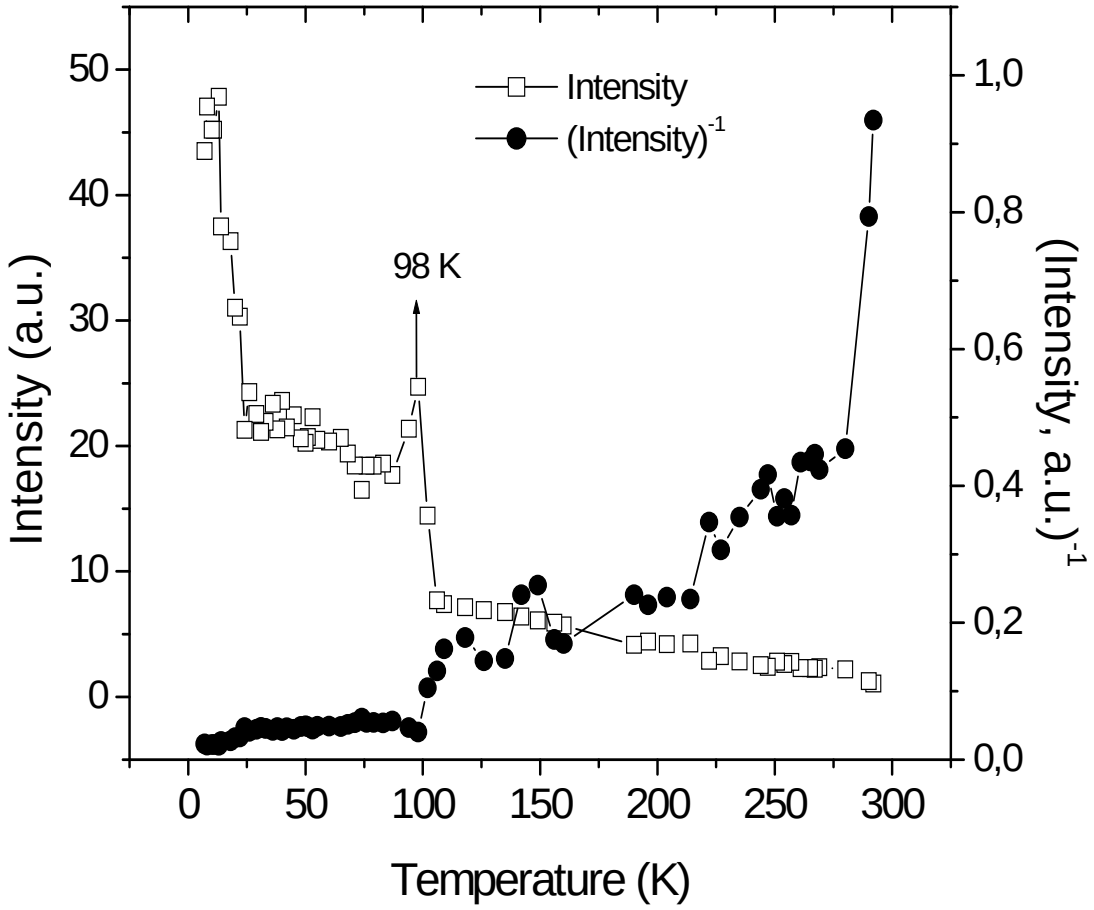

Figure 5.15 Temperature dependence of absorption intensity and inverse intensity for $LaFeO_3$-$LaGaO_3$ with 3 mol % of Fe

CHAPTER 6

CONCLUSION

X-band room and low temperature paramagnetic resonance measurements have revealed the heterovalent structure for both solid solutions of $LiMnO_2$-$LiGaO_2$ (2 mol % of Mn) and $La_{0.75}Sr_{1.25}MnO_4$-$LaSrAlO_4$ (2, 4 mol % of Mn) that include Mn (II, III, IV) ions. The spectrum recorded from $LiMnO_2$-$LiGaO_2$ has a single, symmetric and Lorentzian resonance peak which originates from Mn^{2+} ion until 80 K. Below this temperature, an additional, very broad and intensive peak that arises due dipolar interactions between mainly Mn^{4+} and Mn^{3+}ions. The three magnetic phase transitions were detected around 26, 51 and 80 K due to competition between ferromagnetic and antiferromagnetic exchange interactions. In addition to these exchange correlations, dipolar interactions between like and unlike Mn ions play important role at the line shape, line width and absorption intensities with decreasing temperature. Moreover, the spin-glass like behavior due to cluster formation and magnetic disorder has been detected.

Two intensive resonance peaks, one is shoulder like originates from the Mn^{2+} ions in rhombic symmetry and other is around g = ~2 originates mainly from Mn^{2+} ions in the axial symmetry are recorded from the solid solution of $La_{0.75}Sr_{1.25}MnO_4$-$LaSrAlO_4$. The peak around g = ~2 value includes hyperfine features for the 2 mol % of Mn but hyperfine lines disappear for 4 mol % of Mn due to dipolar interactions. Two remarkable magnetic transitions were recorded around 67 and 105 K. In addition to allowed transitions of Mn^{2+} ion, the forbidden ΔM_S=2 transitions originate from the Mn^{4+} ion were registered below 120 K. By decreasing temperature, the intensity of forbidden transitions increases due to increase at spin-lattice (T_1) and spin-spin (T_2) relaxation times. The exchange and dipolar interactions between Mn^{2+}, Mn^{3+} and Mn^{4+} ions were detected strongly in the temperature range of 30-110 K and caused to large broadening effects on the spectra.

Also for ferrate and perovskite structure solid solutions of $LiFeO_2$-$LiGaO_2$ (5 mol % of Fe), $LiFeO_2$-$LiScO_2$ (5 mol % of Fe) and $LaFeO_3$-$LaGaO_3$ (3 mol % of Fe), x-band room and low temperature paramagnetic resonance measurements have been studied. A very strong resonance peak with g ~ 2 has been observed around room temperature and some minor peaks in the low magnetic field region for $LiFeO_2$-$LiGaO_2$. According to the theoretical fit studies, by using the SimFonia simulation program, a transition from cubic to orthorhombic symmetry which originated from Fe^{3+} ions have been observed [54]. For all ferrate and perovskite type solid solutions, magnetic phase transitions were detected between 25 K and 100 K, because of the ferromagnetic and antiferromagnetic interactions. From the spectra of $LaFeO_3$-$LaGaO_3$, it can be seen that polycrystalline ordering is the major case than the clustering.

REFERENCES

[1]. Y. S. Lee, S. Sato, Y. K. Sun, K. Kobayakawa, Y. Sato, Electrochem. Commun. 5, (2003) 359.

[2]. Y.I. Jang, F.C. Chou, B. Huang, D. R. Sadoway and Y. M. Chiang, *J. Phys. Chem. Solids* 64 (2003), p. 2525.

[3]. Xin-Cun Tang, Cheng-Kui Jiang, Chun-Yue Pan, Bo-Yun Huang and Yue-Hui He, J. Solid State Chem. 179, 4, (2006) 1100.

[4]. J. E. Greedan, N. P. Raju, I. J. Davidson, J. Solid State Chem. 128, (1997) 209.

[5]. Y. M. Chiang, H. Wang, Y. I. Jang, Chem. Mater. 13, (2001) 53.

[6]. H. Wang, Y. I. Jang, Y. M. Chiang, Electrochem. Solid-State Lett. 2, (1999) 490.

[7]. Y. S. Lee, S. Sato, Y. K. Sun, K. Kobayakawa, Y. Sato, J. Power Sources 119-121, (2003) 285.

[8]. Y. Sakurai, H. Arai, J. Yamaki, Solid State Ionics 113-115, (1998) 29.

[9]. M. Tabuchi, S. Tsutsui, C. Masquielier, R. Kanno, K. Ado, I. Matsubara, S. Nasu, H. Kageyama, L. Solid State Chem. 140, (1998) 159.

[10]. R. Kanno, T. Shirane, Y. Kawamoto, Y. Takeda, M. Takano, M. Ohashi, Y. Yamaguchi, J. Electrochem. Soc. 146, (1996) 2435.

[11]. L.G.Tejuca, J. l. G. Fierro (Eds), Properties and Applications of Perovskite- type Oxides, Marcel Dekker, New York, 1993.

[12]. R.L.Garten, R. A. DalleBetta, J. C. Schlatter, in: G. Ertl, H. Knozinger, J. Weitkamp (Eds), Handbook of Heterejeneous Catalysis, Vol. 4, VHC, Weinheim, Germany, 1998, 1668.

[13]. T. Seiyama, Catal. Rev. Sci. Eng. 34, (1992) 281.

[14]. P. Ciambelli, S. Cimino, S. De Rossi, L. Lisi, G. Minelli, P. Porta, G. Russo, Appl. Catal. B 29, (2001) 239.

[15]. C.S. Kim, Y.R. Uhm, S. B. Kim and J.G. Lee, *J. Magn. Magn. Mater.* 215–216, (2000) 551.

[16]. P. Ciambelli, S. Cimino, S. De Rossi, L. Lisi, G. Minelli, P. Porta and G. Russo. *Appl. Catal., B Environ.* 29**,** (2001) 239.

[17]. D. Treves, *Phys. Rev. Lett.* 125, **(**1962) 1843.

[18]. T.C. Gibb. *J. Chem. Soc. Dalton Trans.* (1985) 1455.

[19]. Y.R. Uhm, S.W. Lee, K. Park, Y. Tomioka, Y. Tokura, C. S. Kim, J. Appl. Phys. 87, (2000) 4873.

[20]. U. Russo, L. Nodari, M. Faticanti, V. Kuncser and G. Filoti, *Solid State Ionics* 176, (2005) 97.

[21]. C. Baumann, G. Allodi, A. Amato, B. Buchner, D. Cattani, R. De Renzi, R. Klingeler, P. Reutler, A. Revcolevschi, Physica B 374-375, (2006) 83.

[22]. P. Reutler et al., J. Cryst. Growth 249 (1-2), (2003) 222.

[23]. N. Chezhina, M. Mikhailova, A. Osipova, Solid State Ionics, 141-142, (2001) 617.

[24]. D. Zhu, A. Maignan, M. Hervieu, S. Hébert, B. Raveau, Sol. St. Commun. 127, (2003) 551.

[25]. J. Hu, H. Qin, Mater. Sci. Eng. B 100, (2003) 304.

[26]. Stephen Blundel Magnetism in Condensed Matter, Oxford University Press 2001.

[27]. David J. Griffiths, Introduction to Quantum Mechanics, Prentice Hall, 1995.

[28]. Soshin Chikazumi, Physics of Ferromagnetism, Oxford University Press, Oxford New York, 2. Aufl. (1997)

[29]. A. Abragam and B. Bleaney, Electron Paramagnetic Resonance of Transition Ions (Clarendon Press, Oxford 1982).

[30]. http://www.bruker-biospin.com:80/whatisepr.html?&L=0

[31]. C. N. Banwell, Fundamentals of Molecular Spectroscopy; 2nd ed.; McGraw-Hill Book Company: Maidenhead, U.K., 1972.

[32]. Y. I. Jang, F. C. Chou, B. Huang, D. R. Sadoway, Y. M. Chiang, J. Phys. Chem. Solids 64, (2003) 2525.

[33]. R. R. Rakhimov, A. L. Wilkerson, G. B. Loutts, M.A. Noginov, N. Noginova, W. Lindsay and H. R. Ries, Sol. St. Commun. 108, 8, (1998) 549.

[34]. K. Petrov, R. M. Rojas, P. J. Alonso, J. M. Amarilla, M. G. Lazarraga, J. M. Rojo, Solid State Sciences 7, (2005) 277.

[35]. M. Wakeshema and Y. Hinatsu, J. Solid State Chem. 153, (2000) 330.

[36]. R.P.S. Chakradhar, G. Sivaramaiah, J. L. Rao, N. O. Gopal, Spectrochim. Acta Part A, 62, (2005) 761.

[37]. S. Güner, B. Rameev, B. Aktaş, JMMM 258- 259, (2003) 372.

[38]. B. D. Cullity, Introduction to Magnetic Materials, (Addison-Wesley Publishing Inc., Massachussets, USA, (1972), p. 178.

[39]. M. Kakazey, N. Ivanova, Y. Boldurev, S. Ivanov, G. Sokolsky, J. G. Gonzalez-Rodrigez, M. Vlasova, J. Power Sources 114, (2003) 170.

[40]. C. Zener, Phys. Rev. 118, (1951) 403.

[41]. Y. Köseoğlu, F. Yıldız, G. Salazar-Alvarez, M. Toprak, M. Muhammed and B. Aktaş, Phys. Stat. Sol. B, 242, 8, (2005) 1712.

[42]. D. Ramirez-Rosales, R. Zamorano-Ulloa, O. Perez-Martinez, Sol. St. Commun. 118, (2001) 371.

[43]. S. K. Misra, Physica B, 240 (1997) 183.

[44]. G. Swarnabala, M.V. Rajasekharan, S. Padhye, Chem. Phys. Lett. 267, (1997) 539.

[45]. G. Catana, J. Pelgrims and R. A. Schoonheydt, Zeolites 15, (1995) 475.

[46]. B. Boizot, G. Petite, D. Ghaleb, G. Calas NIM B 141, (1998) 580.

[47]. A. Tavman, Naz M. Agh-Atabay , S. Güner, F. Gucin and B. Dulger, Transition Metal Chemistry, 72, 2, (2007) 172.

[48]. D. Loveridge and S. Parke, *Phys. Chem. Glasses*, 12, (1971) 90.

[49]. D. Goldfarb, M. Bernardo, K. G. Stohmaier, D. E. W. Vaughan and H. Thomann, J. Am. Chem. Soc., 116, (1994) 6344.

[50]. B. V. Padlyak and A. Gutsze, J. Chem. Soc. Faraday Trans., 14, (1998) 59.

[51]. J. L. Rao, A. Murali and E. D. Rao, J. Non-Cryst. Solids, 202, (1996) 215.

[52]. J. Kliava, Phys. Status Solidi B, 134, (1986) 411.

[53]. T. Castner, G. S. Newell Jr., W. C. Holton and C. P. Slichter, J. Chem. Phys., 32, (1960) 668.

[54]. WIN-EPR SimFonia, GmbH; Version 1.25; Copyright 1994-1996.